Progress In Electromagnetics Research, PIER 10, 271–319, 1995

TRANSFER MATRIX METHOD WITH APPLICATIONS TO DISTRIBUTED FEEDBACK OPTICAL DEVICES

T. Makino

1. Introduction

Periodic structures consisting of corrugated waveguides have been used for passive and active optical devices such as grating filters, input and output grating couplers, distributed feedback (DFB) lasers and amplifiers, and distributed Bragg reflector (DBR) lasers [1]. The coupled mode theory (CMT) has extensively been used for the analysis of periodic structures because of its simplicity and flexibility [2]. An important parameter is the coupling coefficient which gives the relative amount of power coupled between two modes per unit length. The coupling coefficient for the TE and TM modes have been evaluated in the scope of coupled mode theory [3,4]. However, the accurate evaluation of the coupling coefficient for the TM mode is difficult because the boundary condition is not satisfied by the conventional coupled mode

solution [4]. Although a few formulations have been developed for the TM modes [5], the accuracy and the scope of validity are still to be verified. Furthermore, the applicability of the conventional two wave coupled mode theory is limited to a shallow corrugation because the theory is based on a perturbation method.

DFB semiconductor lasers are one of the important corrugated waveguide devices. DFB lasers have been used most widely as dynamic single-mode (DSM) light sources in optical fiber communications systems [6]. Most of the theoretical analysis of the longitudinal mode behavior of DFB lasers have been based on the CMT [7]. However, the recent progress of multi-quantum-well (MQW) DFB lasers [8] require a more accurate evaluation of the longitudinal effect of the optical gain of quantum wells because it significantly affects the lasing mode spectrum.

The transfer matrix method (TMM) is another powerful tool for the analysis of periodic structures. The TMM has been used in two different ways. One way is to represent the solution of the coupled mode equations by a 2×2 transfer matrix, which relates the forward- and backward-propagating field amplitudes [9]. Almost-periodic gratings can be analyzed effectively by this method [9]. The grating structure is divided into a number of uniform grating sections which have an analytic transfer matrix. The transfer matrix for the entire structure can be obtained by multiplying the individual transfer matrices together. It should be noted that this method is simply a numerical method for solving the coupled mode equations.

The other way of the TMM is to represent each corrugation section by a transfer matrix [10,11]. The reflection of the propagating modes of a corrugated waveguide at the discontinuity of the corrugation can be described by the discontinuity of the effective index in the same way as plane waves are reflected. Therefore, the transfer matrix of each corrugation section can be expressed in terms of the mode reflection and transmission coefficients and the propagation constant, which is similar to the matrix used in the analysis of thin-film optical filters [12].

Reflection and transmission coefficients are fundamental parameters in periodic waveguide devices. However, in the analysis of DFB and DBR lasers and amplifiers, the spontaneous emission noise generated within a laser cavity has to be taken into account because it affects the mode behavior of lasers and the noise figure of optical

amplifiers [13]. Therefore, more accurate model of spontaneous emission noise is required, which should be based on the TMM [14,15].

In this chapter, the TMM and its application to DFB waveguide structures, especially DFB semiconductor lasers are discussed in detail. This chapter is organized as follows. In Section 2, the transfer matrix for corrugation discontinuities in a corrugated optical waveguide is derived by using the local normal mode. In Section 3, the total transfer matrix of a whole DFB structure is derived analytically in terms of a single-period transfer matrix. Then, the TMM is compared to the CMT. In Section 4, the TMM is extended to incorporate the spontaneous emission noise in semiconductor lasers by combining with the Green's function method. As numerical examples, the TMM is applied to the threshold analysis of bulk active-layer DFB semiconductor lasers and MQW DFB lasers. Then, applications to vertical cavity surface-emitting DFB and DBR lasers are discussed. Finally, conclusions are given in Section 5.

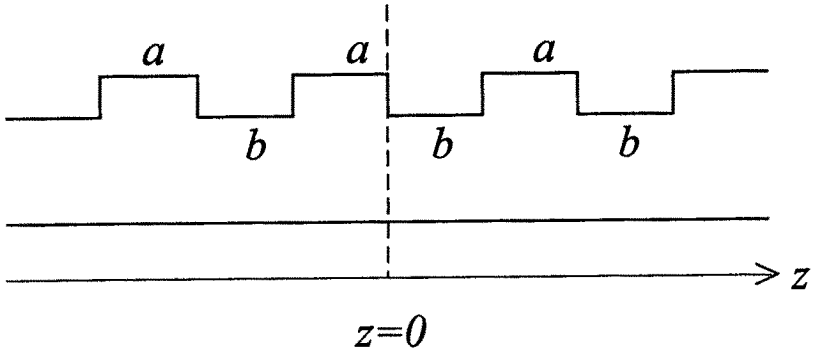

Figure 2.1 Schematic diagram of a single-mode waveguide with a periodic corrugation.

2. Transfer Matrix

Consider a corrugated slab waveguide structure as shown in Fig. 2.1. For simplicity, we assume that the shape of the corrugation is rectangular. The grating sections with larger waveguide thickness and

smaller waveguide thickness are denoted by a and b, respectively, as shown in Fig. 2.1. We also assume that the single transverse mode is retained in the waveguide with the presence of the corrugation. There are two types of discontinuities at the boundary between the sections a and b: one is the discontinuity of the propagation constants of the guided-modes, and the other is discontinuity of the local normal mode profiles. Consider the discontinuity at $z = 0$. For the TE modes, the electric field E_y satisfies the wave equation

$$[\nabla^e + \omega^2/c^2\epsilon(x,y,z)]E_y(x,y,z) = 0 \tag{2.1}$$

$E_y(x,y,z)$ can be written as

$$E_y(x,y,z) = \phi(x,y)F(z) \tag{2.2}$$

where $\phi(x,y)$ is the transverse mode field, and $F(z)$ is the longitudinal dependence. $\phi(x,y)$ satisfies

$$[\partial^2/\partial x^2 + \partial^2/\partial y^2 + \omega^2/c^2\epsilon(x,y,z)]\phi(x,y) = \beta^2\phi(x,y) \tag{2.3}$$

$F(z)$ satisfies

$$(d^2/dz^2 + \beta^2)F(z) = 0 \tag{2.4}$$

where β is the propagation constant. Noting that β is independent of z in the section a, we can write the electric field in the section a as

$$E_{ya} = [E_a^+ \exp(-j\beta_{az}) + E_a^- \exp(j\beta_{az})]\phi_a(x,y) + E_{ra} \tag{2.5a}$$

where E_a^+ and E_a^- are the amplitudes for the forward and backward local normal modes in the section a. Similarly, for the section b, we can write

$$E_{yb} = [E_b^+ \exp(-j\beta_{bz}) + E_b^- \exp(j\beta_{bz})]\phi_b(x,y) + E_{rb} \tag{2.5b}$$

E_b^+ and E_b^- are the corresponding amplitudes in the section b. E_{ra} and E_{rb} are the radiation modes in the sections a and b, respectively. By matching E_y and H_x at $z = 0$, we obtain [16,18]

$$(E_a^+ + E_a^-)\phi_a(x,y) + E_{ra} = (E_b^+ + E_b^-)\phi_b(x,y) + E_{rb} \tag{2.6a}$$

$$\begin{aligned} &-j\beta_a(E_a^+ - E_a^-)\phi_a(x,y) + \partial/\partial z E_{ra}|_{z=0} \\ &= -j\beta_b(E_b^+ - E_b^-)\phi_b(x,y) + \partial/\partial z E_{rb}|_{z=0} \end{aligned} \tag{2.6b}$$

Multiplying both sides of (2.6) by $\phi_a(x,y)$ and then integrating the equation over the transverse plane, we obtain

$$(E_a^+ + E_a^-)\int \phi_a\phi_a dxdy = (E_b^+ + E_b^-)\int \phi_a\phi_b dxdy \tag{2.7a}$$

$$\beta_a(E_a^+ + E_a^-)\int \phi_a\phi_a dxdy = \beta_b(E_b^+ + E_b^-)\int \phi_a\phi_b dxdy \tag{2.7b}$$

where the integral over x for the radiation modes in the section b vanished due to the exact orthogonality relation with the guided mode E_{yb} in this section. The integrals for the radiation modes in the section a do not exactly vanish. However, this was neglected because it is much smaller than other integrals.

From (2.7), we obtain

$$\begin{pmatrix} E_a^+ \\ E_a^- \end{pmatrix} = \begin{pmatrix} \frac{\beta_a+\beta_b}{2\beta_a}\chi_{ab}^{TE} & \frac{\beta_a-\beta_b}{2\beta_a}\chi_{ab}^{TE} \\ \frac{\beta_a-\beta_b}{2\beta_a}\chi_{ab}^{TE} & \frac{\beta_a+\beta_b}{2\beta_a}\chi_{ab}^{TE} \end{pmatrix} \begin{pmatrix} E_b^+ \\ E_b^- \end{pmatrix} \tag{2.8}$$

where

$$\chi_{ab}^{TE} = \frac{\int \phi_a\phi_b dxdy}{\int \phi_a^2 dxdy} \tag{2.9}$$

This expresses the modal shape overlap between the sections a and b.

For the TM modes, we obtain in a similar way [17,18]

$$\begin{pmatrix} E_a^+ \\ E_a^- \end{pmatrix} = \begin{pmatrix} \frac{\beta_a q_a+\beta_b q_b}{2\beta_a q_a}\chi_{ab}^{TM} & \frac{\beta_a q_a-\beta_b q_a}{2\beta_a q_a}\chi_{ab}^{TM} \\ \frac{\beta_a q_a-\beta_b q_b}{2\beta_a q_a}\chi_{ab}^{TM} & \frac{\beta_a q_a+\beta_b q_b}{2\beta_a q_a}\chi_{ab}^{TM} \end{pmatrix} \begin{pmatrix} E_b^+ \\ E_b^- \end{pmatrix} \tag{2.10}$$

with

$$q_a = \int \frac{\phi_a \phi_b}{n_a^2} dxdy \tag{2.11a}$$

$$q_b = \int \frac{\phi_a \phi_b}{n_b^2} dxdy \tag{2.11b}$$

$$\chi_{ab}^{TM} = \frac{\int \frac{\phi_a \phi_b}{n_a^2} dxdy}{\int \frac{\phi_a^2}{n_a^2} dxdy} \tag{2.12}$$

where n_a and n_b are the refractive index distributions of the transverse waveguides for the grating sections a and b, respectively.

Defining the effective index $N_i = \beta_i/k (i = a, b)$ where k is the free-space wavenumber, we can rewrite (2.8) and (2.10) as

$$\begin{pmatrix} E_a^+ \\ E_a^- \end{pmatrix} = \boldsymbol{D_{ab}} \begin{pmatrix} E_b^+ \\ E_b^- \end{pmatrix} = \begin{pmatrix} 1/t_{ab} & r_{ab}/t_{ab} \\ r_{ab}/t_{ab} & 1/t_{ab} \end{pmatrix} \begin{pmatrix} E_b^+ \\ E_b^- \end{pmatrix} \tag{2.13}$$

where

$$t_{ab} = \begin{cases} \dfrac{2N_a}{N_a + N_b} \cdot \dfrac{1}{\chi_{ab}^{TE}} & \text{for TE modes} \\ \dfrac{2N_a q_a}{N_a q_a + N_b q_b} \cdot \dfrac{1}{\chi_{ab}^{TM}} & \text{for TM modes} \end{cases} \tag{2.14a}$$

$$r_{ab} = \begin{cases} \dfrac{N_a - N_b}{N_a + N_b} & \text{for TE modes} \\ \dfrac{N_a q_a - N_b q_b}{N_a q_a + N_b q_b} & \text{for TM modes} \end{cases} \tag{2.14b}$$

Similarly, we obtain from (2.6)

$$\begin{pmatrix} E_b^+ \\ E_b^- \end{pmatrix} = \boldsymbol{D_{ba}} \begin{pmatrix} E_a^+ \\ E_a^- \end{pmatrix} = \begin{pmatrix} 1/t_{ba} & r_{ba}/t_{ba} \\ r_{ba}/t_{ba} & 1/t_{ba} \end{pmatrix} \begin{pmatrix} E_a^+ \\ E_a^- \end{pmatrix} \tag{2.15}$$

with

$$t_{ba} = \begin{cases} \frac{2N_b}{N_a + N_b} \cdot \frac{1}{\chi_{ba}^{TE}} & \text{for TE modes} \\ \frac{2N_b q_b}{N_a q_a + N_b q_b} \cdot \frac{1}{\chi_{ba}^{TM}} & \text{for TM modes} \end{cases} \tag{2.16a}$$

$$r_{ba} = \begin{cases} \frac{N_b - N_a}{N_b + N_a} & \text{for TE modes} \\ \frac{N_b q_b - N_a q_a}{N_b q_b + N_a q_a} & \text{for TM modes} \end{cases} \tag{2.16b}$$

$$\chi_{ba}^{TE} = \frac{\int \phi_a \phi_b dx dy}{\int \phi_b^2 dx dy} \tag{2.17a}$$

$$\chi_{ba}^{TM} = \frac{\int \frac{\phi_b \phi_a}{n_b^2} dx dy}{\int \frac{\phi_b^2}{n_b^2} dx dy} \tag{2.17b}$$

The form of Eq. (2.13) or (2.15) is exactly the same as the transfer matrix in thin film optics [12]. Therefore, the corrugated waveguide structure can be reduced to a 1D stacked-layer structure consisting of alternating layers with effective indices N_a and N_b as shown in Fig. 2.2.

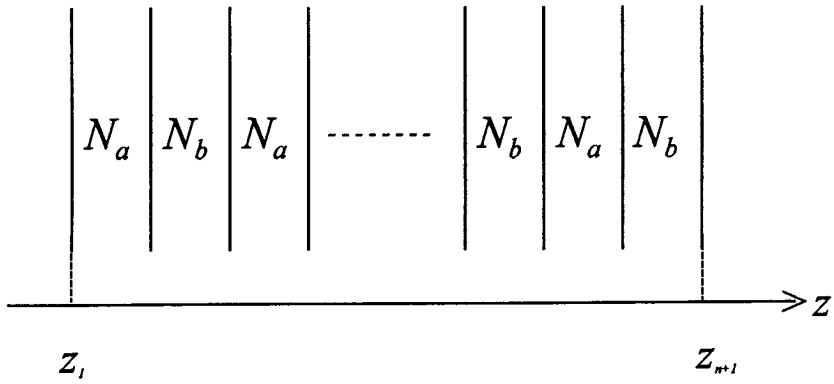

Figure 2.2 Transformed on-dimensional periodic structure.

The transfer matrix of the uniform region in the section a or b is expressed as

$$\boldsymbol{U_i} = \begin{pmatrix} \exp(-j\beta_i\Lambda_i) & 0 \\ 0 & \exp(j\beta_i\Lambda_i) \end{pmatrix} \qquad (i = a, b) \tag{2.18}$$

Therefore, the transfer matrix for the section $i(i = a, b)$ including the discontinuity and the uniform region is written as

$$\boldsymbol{T_a} = \boldsymbol{U_a D_{ab}} = \begin{pmatrix} \exp(-j\beta_a\Lambda_a) & 0 \\ 0 & \exp(j\beta_a\Lambda_a) \end{pmatrix} \begin{pmatrix} 1/t_{ab} & r_{ab}/t_{ab} \\ r_{ab}/t_{ab} & 1/t_{ab} \end{pmatrix} \tag{2.19}$$

$$\boldsymbol{T_b} = \boldsymbol{U_b D_{ba}} = \begin{pmatrix} \exp(-j\beta_b a\Lambda_b) & 0 \\ 0 & \exp(j\beta_b\Lambda_b) \end{pmatrix} \begin{pmatrix} 1/t_{ba} & r_{ba}/t_{ba} \\ r_{ba}/t_{ba} & 1/t_{ba} \end{pmatrix} \tag{2.20}$$

We denote the transfer matrix for the kth section by $\boldsymbol{T^{(k)}}$ (see Figure 2.3). Then, the field at $z = z_{1-}$ and the field at $z = z_{n+1+}$ are related by

$$\begin{pmatrix} E_0^+ \\ E_0^- \end{pmatrix} = \boldsymbol{H^{(n)}} \begin{pmatrix} E_{n+1}^+ \\ E_{n+1}^- \end{pmatrix} \tag{2.21}$$

$$\boldsymbol{H^{(n)}} = \boldsymbol{T^{(1)}} \ldots \boldsymbol{T^{(n)}} \tag{2.22}$$

The reflection coefficient R and the transmission coefficient T are given by

$$R \equiv \left.\frac{E_0^-}{E_0^+}\right|_{E_{n+1}^-=0} = -\frac{H_{21}^{(n)}}{H_{22}^{(n)}} \tag{2.23a}$$

$$T \equiv \left.\frac{E_{n+1}^+}{E_0^+}\right|_{E_{n+1}^-=0} = \frac{H_{11}^{(n)}H_{22}^{(n)} - H_{12}^{(n)}H_{21}^{(n)}}{H_{22}^{(n)}} \tag{2.23b}$$

3. Periodic Structures

3.1 Transfer Matrix of Periodic Structures.

If the grating consists of a periodic structure with alternating transfer matrices $\boldsymbol{T_a}$ and $\boldsymbol{T_b}$, the transfer matrix for one period is from Eqs. (2.19) and (2.20)

$$\boldsymbol{T_p} = \boldsymbol{T_a}\,\boldsymbol{T_b} = \frac{1}{t_{ab}t_{ba}} \begin{pmatrix} e_a^{-1}e_b^{-1} - r^2 e_a^{-1}e_b & r(e_a^{-1}e_b - e_a^{-1}e_b^{-1}) \\ r(e_a e_b^{-1} - e_a e_b) & e_a e_b - r^2 e_a e_b^{-1} \end{pmatrix} \tag{3.1}$$

where

$$r = r_{ab} = -r_{ba} \tag{3.2a}$$

$$e_a \equiv \exp(j\beta_a \Lambda_a), \qquad e_b \equiv \exp(j\beta_b \Lambda_b) \tag{3.2b}$$

(3.1) gives

$$\det \boldsymbol{T_p} = T_{p11}T_{p22} - T_{p12}T_{p21} = \chi_{ab}^m \chi_{ba}^m \qquad (m = TE, TM) \tag{3.3}$$

If the structure consists of M periods, the transfer matrix of the entire structure is given by $\boldsymbol{T_p}^M$.

For the TE modes in the grating with a relatively small depth of corrugations, the modal shape discontinuity is small, and, therefore, $\chi_{ab}^{TE}\chi_{ba}^{TE} \approx 1$, giving $\det \boldsymbol{T_p} = 1$. Therefore, the matrix $\boldsymbol{T_p}$ is unimodular. The M th power of a unimodular matrix $\boldsymbol{T_p}$ can be simplified by the following matrix identity [19]

$$\begin{pmatrix} T_{p11} & T_{p12} \\ T_{p21} & T_{p22} \end{pmatrix}^M = \begin{pmatrix} T_{p11}U_{M-1} - U_{M-2} & T_{p12}U_{M-1} \\ T_{p21}U_{M-1} & T_{p22}U_{M-1} - U_{M-2} \end{pmatrix} \tag{3.4}$$

where U_M is the Chebycheff polynomial of the second kind of order M, given as

$$U_M = \frac{\sinh(M+1)\xi\Lambda}{\sinh \xi\Lambda} \tag{3.5}$$

and ξ is given by

$$\cosh \xi\lambda = \frac{T_{p11} + T_{p22}}{2} \tag{3.6}$$

$\Lambda = \Lambda_a + \Lambda_b$ is the period.

When $\boldsymbol{T_p}$ is not unimodular, we shall take a different approach to derive $\boldsymbol{T_p}^M$. $\boldsymbol{T_p}$ can be diagonalized by finding a suitable matrix $\mathbf{S}$ as [18]

$$\mathbf{S}^{-1}\mathbf{T}_\mathbf{p}\mathbf{S} = \mathbf{\Gamma} \tag{3.7}$$

with

$$\mathbf{\Gamma} = \begin{pmatrix} \exp(\gamma_1\Lambda) & 0 \\ 0 & \exp(\gamma_2\Lambda) \end{pmatrix} \tag{3.8}$$

where $\exp(\gamma_1\Lambda)$ and $\exp(\gamma_2\Lambda)$ are the eigenvalues of $\boldsymbol{T_p}$ given by

$$\exp(\gamma_1\Lambda) = \frac{T_{p11} + T_{p22}}{2} + \sqrt{\left(\frac{T_{p11} + T_{p22}}{2}\right)^2 + T_{p12}T_{p21} - T_{p11}T_{p22}} \tag{3.9a}$$

$$\exp(\gamma_2\Lambda) = \frac{T_{p11} + T_{p22}}{2} - \sqrt{\left(\frac{T_{p11} + T_{p22}}{2}\right)^2 + T_{p12}T_{p21} - T_{p11}T_{p22}} \tag{3.9}$$

If $\det \boldsymbol{T_p} = T_{p11}T_{p22} - T_{p12}T_{p21} = 1$, then we get $\gamma_1 = -\gamma_2$. It can easily be confirmed that γ_1 satisfies (3.6) ($\gamma_1 = -\gamma_2 = \xi$). The elements S_{ij} of $\boldsymbol{S}$ can be obtained as the eigenvectors (S_{11}, S_{12}) and (S_{12}, S_{22}) corresponding to the eigenvalues $\exp(\gamma_1\Lambda)$ and $\exp(\gamma_2\Lambda)$, respectively:

$$(T_{p11} - e^{\gamma_1\Lambda})S_{11} + T_{p12}S_{p21} = 0 \tag{3.10a}$$

$$T_{p21}S_{12} + (T_{p22} - e^{\gamma_2\Lambda})S_{22} = 0 \tag{3.10b}$$

We obtain from (3.10)

$$\frac{S_{21}}{S_{11}} = -\frac{T_{p11} - T_{p22}}{2T_{p12}} + \sqrt{\left(\frac{T_{p11} - T_{p22}}{2T_{p12}}\right)^2 + \frac{T_{p21}}{T_{p12}}} \tag{3.11a}$$

$$\frac{S_{12}}{S_{22}} = \frac{T_{p12}}{T_{p21}}\left(\frac{T_{p11}-T_{p22}}{2T_{p12}} - \sqrt{\left(\frac{T_{p11}-T_{p22}}{2T_{p12}}\right)^2 + \frac{T_{p21}}{T_{p12}}}\right) \tag{3.11b}$$

Defining

$$\sin\psi = \frac{T_{p11}-T_{p22}}{2T_{p12}}e_a^{-1} \tag{3.12}$$

and noting from (3.1)

$$T_{p21}/T_{p12} = -e_a^2 \tag{3.13}$$

$$S_{21}/S_{11} = je_a e^{j\psi} \tag{3.14a}$$

$$S_{12}/S_{22} = je_a^{-1}e^{j\psi} \tag{3.14b}$$

Therefore, we can express $\boldsymbol{S}$ as

$$\boldsymbol{S} = \frac{1}{\sqrt{1+(e^{j\psi})^2}}\begin{pmatrix} 1 & je_a^{-1}e^{j\psi} \\ je_a e^{j\psi} & 1 \end{pmatrix} \tag{3.15}$$

We can rewrite (3.8) as

$$\boldsymbol{\Gamma} = e^{(\gamma_1+\gamma_2)\Lambda/2}\begin{pmatrix} e^{(\gamma_1-\gamma_2)\Lambda/2} & 0 \\ 0 & e^{-(\gamma_1-\gamma_2)\Lambda/2} \end{pmatrix} \tag{3.16}$$

(3.9) gives

$$e^{(\gamma_1+\gamma_2)\Lambda/2} = (\det\ \boldsymbol{T_p})^{1/2} \tag{3.17}$$

We define a new parameter

$$\gamma = \frac{\gamma_1-\gamma_2}{2} \tag{3.18}$$

Then, $\boldsymbol{\Gamma}$ in (3.16) can be expressed as

$$\boldsymbol{\Gamma} = (\det\ \boldsymbol{T_p})^{1/2}\begin{pmatrix} e^{\gamma\Lambda} & 0 \\ 0 & e^{-\gamma\Lambda} \end{pmatrix} \tag{3.19}$$

Using (3.9) in (3.18), we obtain

$$\tanh^2 \gamma\Lambda = \left(\frac{T_{p11} - T_{p22}}{T_{p11} + T_{p22}}\right)^2 - \left(\frac{2e_a T_{p12}}{T_{p11} + T_{p22}}\right)^2 \tag{3.20}$$

(3.12) and (3.20) give

$$\cos\psi = -je_a^{-1}\left(\frac{T_{p11} + T_{p22}}{2T_{p12}}\right)\tanh\gamma\Lambda \tag{3.21}$$

From (3.7), we obtain

$$\boldsymbol{T_p} = \boldsymbol{S}\,\boldsymbol{\Gamma}\,\boldsymbol{S}^{-1} \tag{3.22}$$

If one makes a transformation by letting

$$\begin{pmatrix} E^+ \\ E^- \end{pmatrix} = \boldsymbol{S}\begin{pmatrix} E'^+ \\ E'^- \end{pmatrix} \tag{3.23}$$

Then, the transfer matrix which links E_+ and E_- at the two ends of one period can be obtained from (3.7)

$$\begin{pmatrix} E'^+(n\Lambda + \Lambda) \\ E'^-(n\Lambda + \Lambda) \end{pmatrix} = \boldsymbol{\Gamma}\begin{pmatrix} E'^+(n\Lambda) \\ E'^-(n\Lambda) \end{pmatrix} \tag{3.24}$$

Therefore E'^+ and E'^- represent the amplitudes of the two dominant Bloch waves in this structure. If the structure consists of M periods, the total transfer matrix is

$$\boldsymbol{T_p}^M = (\boldsymbol{S}\,\boldsymbol{\Gamma}\,\boldsymbol{S}^{-1})^M = \boldsymbol{S}\boldsymbol{\Gamma}^M\boldsymbol{S}^{-1} \tag{3.25}$$

Using (3.18) and (3.22), we can express $\boldsymbol{T_p}^M$ as

$$\boldsymbol{T_p}^M = \frac{(\det \boldsymbol{T_p})^{M/2}}{1 + e^{j2\psi}} \cdot \begin{pmatrix} e^{\gamma M\Lambda} + e^{j2\psi}e^{-\gamma M\Lambda} & -je_a^{-1}e^{j\psi}(e^{\gamma M\Lambda} - e^{-\gamma M\Lambda}) \\ je_a e^{j\psi}(e^{\gamma M\Lambda} - e^{-\gamma M\Lambda}) & e^{-\gamma M\Lambda} + e^{j2\psi}e^{\gamma M\Lambda} \end{pmatrix} \tag{3.26}$$

The reflection coefficient at the input end is obtained from (2.23a) as

$$R = \frac{-je_a \sinh \gamma M\Lambda}{\cosh(\gamma M\Lambda + \psi)} \tag{3.27}$$

γ is given by (3.20), and ψ is given by (3.12).

The phase matching condition is

$$\mathrm{Re}(\beta_a \Lambda_a) = \frac{\pi}{2} \tag{3.28a}$$

$$\mathrm{Re}(\beta_b \Lambda_b) = \frac{\pi}{2} \tag{3.28b}$$

where the symbol Re stands for the real party of a complex number. The total grating period of the DFB structure is

$$\Lambda = \Lambda_a + \Lambda_b = \frac{\pi}{2\mathrm{Re}(\beta_a)} + \frac{\pi}{2\mathrm{Re}(\beta_b)} \tag{3.29}$$

Under the phase matching condition, we can approximate e_a and e_b in (3.2b) as

$$e_a = e_b = j \tag{3.30}$$

Then, (3.20) gives

$$\gamma = \gamma_0 = \frac{\tanh^{-1} 2r}{\Lambda} \tag{3.31}$$

(3.12) gives

$$\psi = 0 \tag{3.32}$$

Therefore, (3.27) gives the input reflection coefficient at the Bragg frequency

$$R = \tanh \gamma_0 M\Lambda \tag{3.33}$$

3.2 Comparison to the Coupled Mode Theory.

The propagation constant β in equation (2.4) can be approximated by

$$\beta(z) = \beta_{av} + 2\kappa \cos(2\beta_0 z + \phi) \tag{3.34}$$

where β_{av} is the average wavenumber, κ is the coupling coefficient of the grating, ϕ is the phase of the grating at $z = 0$, β_0 is the Bragg wavenumber. A solution of (2.4) can be written in the form

$$E(z) = R(z)\exp(-j\beta_0 z) + S(z)\exp(j\beta_0 z) \tag{3.35}$$

where $R(z)$ and $S(z)$ satisfy the coupled equations [2][7]

$$-\frac{dR(z)}{dz} + (\alpha - j\delta)R(z) = j\kappa \exp(-j\phi)S(z) \tag{3.36a}$$

$$\frac{dS(z)}{dz} + (\alpha - j\delta)S(z) = j\kappa \exp(j\phi)R(z) \tag{3.36b}$$

$\alpha = \mathrm{Im}(\beta_{av})$ is the average modal gain, and δ is the deturning from the Bragg frequency. The solution of (3.36) is expressed as

$$R(z) = A \exp(\gamma' z) + \beta\rho \exp(-\gamma' z) \tag{3.37a}$$

$$S(z) = A\rho \exp(\gamma z) + \beta \exp(-\gamma z) \tag{3.37b}$$

where

$$\rho = \frac{j\kappa}{\gamma' - j\delta} = j\frac{\gamma' + j\delta}{\kappa} \tag{3.38}$$

γ' is the propagation constant given by

$$\gamma'^2 = \kappa^2 - \delta^2 \tag{3.39}$$

Equation (3.37) can be expressed in a matrix form as

$$\begin{pmatrix} R(z) \\ S(z) \end{pmatrix} = \begin{pmatrix} T_{11}(z|z_a) & T_{12}(z|z_a) \\ T_{21}(z|z_a) & T_{22}(z|z_a) \end{pmatrix} \begin{pmatrix} R(z_a) \\ S(z_a) \end{pmatrix} \tag{3.40}$$

where z_a is an arbitrary vowel of z. The matrix elements are [13]

$$T_{11}(z|z_a) = (F - \rho^2 F^{-1})/(1 - \rho^2) \tag{3.41a}$$

$$T_{12}(z|z_a) = -\rho(F - F^{-1})e^{-j\phi}/(1 - \rho^2) \tag{3.41b}$$

$$T_{21}(z|z_a) = \rho(F - F^{-1})e^{j\phi}/(1 - \rho^2) \tag{3.41c}$$

$$T_{22}(z|z_a) = (F^{-1} - \rho^2 F)/(1 - \rho^2) \tag{3.41d}$$

where

$$F \equiv \exp[\gamma'(z - z_a)] \tag{3.42}$$

The reflection coefficient at the input end is given from (2.23a) by

$$R = \frac{\rho(F - F^{-1})}{\rho^2 F - F^{-1}} \tag{3.43}$$

Under the phase matching condition $\delta = 0$, (3.43) yields

$$R = \tanh \kappa L \tag{3.44}$$

where $\gamma' = \kappa$ and $L = z - z_a$ is the grating length of the DFB structure. Comparing (3.33) and (3.34), we can notice that γ_0 corresponds to the coupling coefficient. Therefore, we can define the coupling coefficient in the TMM by [18]

$$\kappa_{TMM} = \frac{\tanh^{-1} 2r}{\Lambda} \tag{3.45}$$

where r is given by (2.14b). If r is small, κ_{TMM} can be approximated as

$$\kappa_{TMM} = \frac{r}{\Lambda/2} \tag{3.46}$$

Next, decompose the matrix in (3.41) as

$$\begin{aligned}
&\begin{pmatrix} T_{11}(z|z_a) & T_{12}(z|z_a) \\ T_{21}(z|z_a) & T_{22}(z|z_a) \end{pmatrix} \\
&= \frac{1}{\sqrt{1-\rho^2}} \begin{pmatrix} 1 & \rho e^{-j\phi} \\ \rho e^{j\phi} & 1 \end{pmatrix} \begin{pmatrix} e^{\gamma' L} & 0 \\ 0 & e^{-\gamma' L} \end{pmatrix} \\
&\quad \cdot \frac{1}{\sqrt{1-\rho^2}} \begin{pmatrix} 1 & -\rho e^{-j\phi} \\ -\rho e^{j\phi} & 1 \end{pmatrix}
\end{aligned} \tag{3.47}$$

where $L = z - z_a$ is the length of the grating region. It is noted that the matrix $\boldsymbol{T}(z|z_a)$ consists of three matrices; one matrix corresponding to a uniform section with the length L and the propagation constant γ', and two matrices expressing the DFB reflection which is represented by ρ. This means that ρ is an equivalent DFB reflection

coefficient which is similar to the reflection coefficient at the interface discontinuity (see (2.13)). Therefore, the grating can be modeled as if it were a uniform medium with two mirrors at both ends.

The transfer matrix $\boldsymbol{T_p}^M$ in (3.25) can be expressed with use of (3.15) as

$$\begin{aligned}\boldsymbol{T_p}^M = & \frac{1}{\sqrt{1-R_{DFB}^2}} \begin{pmatrix} 1 & R_{DFB}e_a^{-1} \\ R_{DFB}e_a & 1 \end{pmatrix} \\ & \cdot (\det T_p)^{M/2} \begin{pmatrix} e^{\gamma M\Lambda} & 0 \\ 0 & e^{-\gamma M\Lambda} \end{pmatrix} \\ & \cdot \frac{1}{\sqrt{1-R_{DFB}^2}} \begin{pmatrix} 1 & -R_{DFB}e_a^{-1} \\ -R_{DFB}e_a & 1 \end{pmatrix} \end{aligned} \tag{3.48}$$

with

$$R_{DFB} = je^{j\psi} \tag{3.49}$$

We can notice that $\boldsymbol{T_p}^M$ consists of three matrices which are similar to those in (3.47) except $(\det \boldsymbol{T_p})^{M/2}$. Therefore, R_{DFB} corresponds to ρ. We will show that R_{DFB} reduces to exactly the same form as ρ when the grating feedback is weak as follows. Using the deturning factor δ, we the overall phase shift within one period can be written as

$$\beta_a\Lambda_a + \beta_a\Lambda_a = \pi + \delta\Lambda \tag{3.50}$$

Using (3.50) in (3.20), we obtain

$$\tanh^2 \gamma\Lambda = (2r)^2 - \sin^2 \delta\Lambda \tag{3.51}$$

Assume that δ and r are small. Noting (3.45), we can approximate (3.51) as

$$\gamma^2 = \kappa_{TMM}^2 - \delta^2 \tag{3.52}$$

This is exactly the same form as (3.39). Then, (3.12) can be approximated as

$$\sin\psi = \frac{\sin\delta\Lambda}{2r} = \frac{\delta}{\kappa_{TMM}} \tag{3.53}$$

(3.21) can be approximated as

$$\cos\psi = \frac{\tanh\gamma\Lambda}{2r} = \frac{\gamma}{\kappa_{TMM}} \tag{3.54}$$

Therefore, R_{DFB} in (3.49) can be expressed as

$$R_{DFB} = j(\cos\psi + j\sin\psi) = j\frac{\gamma + j\delta}{\kappa_{TMM}} \tag{3.55}$$

Comparing (3.55) with (3.38), we can notice that R_{DFB} reduces to the same form as ρ if κ and γ' are replaced by κ_{TMM} and γ, respectively.

4. Application to Semiconductor Lasers

Consider a very general laser structure consisting of n stacked-layers with each layer having uniform refractive index and carrier density, as shown in Fig. 4.1. This structure obviously models vertical cavity stacked-layer lasers [27–30], in which each segment corresponds to one epitaxial layer. If each segment is chosen such that it corresponds to one part of the corrugation period, this structure can model DFB lasers. A 3D DFB laser structure can be modeled as one special case of the DFB laser structure, consisting of a uniform gain region and a passive grating region.

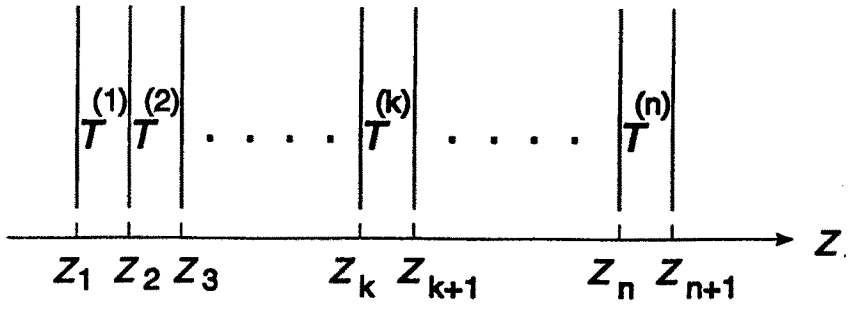

Figure 4.1 Schematic diagram of a stacked multi-layer structure.

According to Henry [20], the laser field can be regarded as an amplified spontaneous emission. In other words, the field is expressed by a solution of the inhomogeneous wave equation with a field source (Langevin force).

In this section, following Henry [20], first we express the field generated by this source in terms of the Wronskian. Next, we express the Wronskian in terms of the transfer-matrix elements.

4.1 Amplified Spontaneous Emission.

A. Field generated by spontaneous emission

We assume that waves propagate along the z axis. r_L and r_R denote the left and right facet reflectivities. We denote by $E(x,y,z,t)$ the transverse electric field component with polarization vector in the $x-y$ plane. The laser waveguide is assumed to be index-guided. If we define the Fourier transform $E_\omega(x,y,z)$ of $E(x,y,z,t)$ by

$$E_\omega(x,y,z) = \int_{-\infty}^{\infty} E(x,y,z,t)e^{-j\omega t}dt \tag{4.1}$$

Then $E_\omega(x,y,z)$ satisfies [20]

$$[\nabla^2 + \omega^2/c^2\epsilon_\omega(x,y,z)]E_\omega(x,y,z) = F_\omega(x,y,z) \tag{4.2}$$

where $F_\omega(x,y,z)$ is the Langevin source.

We assume the laser oscillates in the fundamental transverse mode $\phi_0(x,y)$, which is normalized to satisfy

$$\int |\phi_0(x,y)|^2 dxdy = 1 \tag{4.3}$$

We can write

$$E_\omega(x,y,z) = \phi_0(x,y)E_\omega(z) \tag{4.4}$$

where $E_\omega(z)$ is the complex longitudinal electric field. It can be shown that $E_\omega(z)$ satisfies the inhomogeneous wave equation

$$[d^2/dz^2 + k^2(z)]E_\omega(z) = f_\omega(z) \tag{4.5}$$

where

$$f_\omega(z) = \int F_\omega(x)\phi_0^*(x,y)dxdy \tag{4.6}$$

The solution to (4.5) is given by

$$E_\omega(z) = \int_{z_1}^{z_{n+1}} G(z, z') f_\omega(z') dz' \tag{4.7}$$

where $G(z, z')$ is the Green's function. It has been shown that $G(z, z')$ is given as [20]

$$G(z, z') = \begin{cases} \frac{Z_R(z) Z_L(z')}{W} & z > z' \\ \frac{Z_R(z') Z_L(z)}{W} & z < z' \end{cases} \tag{4.8}$$

where $Z_L(z)$ and $Z_R(z)$ are the solutions of the homogeneous part of (4.5), satisfying the boundary conditions at z_1 and z_{n+1}, respectively. The Wronskian W is defined by

$$W = \frac{dZ_R}{dz} Z_L - Z_R \frac{dZ_L}{dz} \tag{4.9}$$

Substitution of (4.8) into (4.7) yields

$$E_\omega(z) = Z_R(z) \int_{z_1}^{z} \frac{Z_L(z') f_\omega(z')}{W} dz' + Z_L(z) \int_{z}^{z_{n+1}} \frac{Z_R(z') f_\omega(z')}{W} dz' \tag{4.10}$$

This gives the field generated by spontaneous emission. Using (4.10), the average noise power emitted from the facet at $z = z_{n+1}$ within frequency interval $\Delta\omega$ can be calculated as [20]

$$P_R \Delta\omega = \frac{\Delta\omega \hbar \omega^2}{\pi c} \left(-j Z_R(z_{n+1}) \frac{dZ_R^*}{dz}(z_{n+1}) + c.c. \right) \cdot \int_{z_1}^{z_{n+1}} \frac{n_{sp} n' g |Z_L(z)|^2}{|W|^2} dz \tag{4.11}$$

B. Transfer matrix representation.

The transfer matrix in the kth section $\boldsymbol{T}^{(k)}(z|z_k)$ which transforms the traveling-wave electric fields at z_k to those at z ($z_k \leq z \leq z_{k+1}$) is expressed as (see (2.19))

$$\boldsymbol{T}^{(k)}(z|z_k) = \begin{bmatrix} e^{-j\beta_k(z-z_k)} & 0 \\ 0 & e^{j\beta_k(z-z_k)} \end{bmatrix} \begin{bmatrix} 1/t_k & r_k/t_k \\ r_k/t_k & 1/t_k \end{bmatrix} \tag{4.12}$$

where β_k is the complex propagation constant of the k th section, and r_k and t_k are the reflection and transmission coefficients at the interface between the $(k-1)$ th layer and the k th layer. We can express $Z_L(z)$ and $Z_R(z)$ as follows [14].

$$Z_i(z) = Z_{ik}(z) \qquad \text{for } z_k \le z \le z_{k+1} \qquad (i = L, R, k = 1, \cdots, n) \tag{4.13a}$$

$$Z_{ik}(z) = Z_{ik}^{+}(z) + Z_{ik}^{-}(z) \tag{4.13b}$$

$$Z_{Lk}^{+}(z) = T_{12}^{(k1)}(z|z_1) + r_L T_{11}^{(k1)}(z|z_1) \tag{4.14a}$$

$$Z_{Lk}^{-}(z) = T_{22}^{(k1)}(z|z_1) + r_L T_{21}^{(k1)}(z|z_1) \tag{4.14a}$$

$$Z_{Rk}^{+}(z) = Z_{Ln}^{+}(z_{n+1})[T_{11}^{(kn)}(z|z_{n+1}) + r_R T_{12}^{(kn)}(z|z_{n+1})] \tag{4.16a}$$

$$Z_{Rk}^{-}(z) = Z_{Ln}^{+}(z_{n+1})[T_{21}^{(kn)}(z|z_{n+1}) + r_R T_{22}^{(kn)}(z|z_{n+1})] \tag{4.16b}$$

where r_L and r_R are the the facet reflectivities at z_1 and z_{n+1}, respectively, and $T_{ij}^{(k1)}(z|z_1)$ and $T_{ij}^{(kn)}(z|z_{n+1})$ are the elements of the matrices defined by

$$\boldsymbol{T}^{(k1)}(z|z_1) \equiv \boldsymbol{T}^{(k)}(z|z_k)\,\boldsymbol{T}^{(k-1)}(z_k|z_{k-1}) \cdots \boldsymbol{T}^{(1)}(z_2|z_1) \tag{4.17a}$$

$$\boldsymbol{T}^{(kn)}(z|z_{n+1}) \equiv \boldsymbol{T}^{(k)}(z|z_{k+1})\,\boldsymbol{T}^{(k+1)}(z_{k+1}|z_{k+2}) \cdots \boldsymbol{T}^{(n)}(z_n|z_{n+1}) \tag{4.17b}$$

The factor $Z_{Ln}^{+}(z_{n+1})$ in (4.16) ensures that $Z_L(z) = Z_R(z)$ at threshold [14]. It can be shown that the Wronskian W is expressed as [14]

$$W = W_k \qquad \text{for} \qquad z_k \le z \le z_{k+1} \tag{4.18a}$$

$$W_k = j2\beta_k Z_{Ln}^{+}(z_{n+1})[r_R Z_{Ln}^{+}(z_{n+1}) - Z_{Ln}^{-}(z_{n+1})] \tag{4.18b}$$

with

$$Z_{Ln}^{+}(z_{n+1}) = H_{12}^{(n)} + r_L H_{11}^{(n)} \tag{4.19a}$$

$$Z_{Ln}^{-}(z_{n+1}) = H_{22}^{(n)} + r_L H_{21}^{(n)} \tag{4.19a}$$

where $H_{ij}^{(n)}$ is the matrix element of the total transfer matrix $H^{(n)}$ defined as

$$\boldsymbol{H}^{(n)} \equiv \boldsymbol{T}^{(n)} \ldots \boldsymbol{T}^{(1)} \tag{4.20}$$

where $\boldsymbol{T}^{(k)} \equiv \boldsymbol{T}^{(k)}(z_{k+1}|z_k)$ is the transfer matrix of the whole k th section.

4.2 Lasing Condition.

The Wronskian W is a function of the complex wavenumber which is a function of the real angular frequency ω and the optical gain. As the injection current increases, the carrier density increases, and therefore the gain increases, causing the decrease of $|W|$, i.e., the increase of $|E_\omega(z)|$. Threshold is reached when W is nearly equal to zero: The longitudinal mode is described by a zero point of W in a good approximation. Therefore, the threshold condition is expressed by

$$W(\omega_0, g_{1th}, g_{2th}, \ldots, g_{nth}) = 0 \tag{4.21}$$

where ω_0 is the lasing frequency and g_{kth} is the threshold gain of the k th section $(k = 1, 2, \ldots, n)$. Since the optical gain g_k is a function of the carrier density N_k, (4.21) can be expressed as

$$W(\omega_0, N_{1th}, N_{2th}, \ldots, N_{nth}) = 0 \tag{4.22}$$

We see from (4.9) that at $W(\omega_0) = 0$, the functions $Z_L(z)$ and $Z_R(z)$ are proportional to one another. We can choose $Z_L(z)$ and $Z_R(z)$ such that $Z_L(z)$ becomes equal to $Z_R(z)$ when $W = 0$ is reached [20]. Then, (4.10) can be written as

$$E_\omega(z) = A_\omega Z_L(z) \tag{4.23}$$

where

$$A_\omega = \int_{Z_1}^{Z_{n+1}} \frac{Z_L(z') f_\omega(z')}{W} dz' \tag{4.24}$$

$E_\omega(z)$ is therefore proportional to $Z_L(z)$, and hence is also proportional to $Z_R(z)$.

Above threshold, the carrier density is affected by the light intensity, and the laser field is very sensitive to changes in the carrier density. The dynamic interaction of the carrier density and the light intensity is conveniently described by the rate equations for these parameters. The rate equations can be derived by expanding W around the operating points ω_0 and the threshold carrier densities $N_{kth}(k = 1, 2, \ldots, n)$ [35]. This is beyond the scope of this chapter.

The condition (4.22) is expressed in terms of the elements of the total matrix $\boldsymbol{H}^{(n)}$ given by (4.20) as

$$r_R[H_{12}^{(n)} + r_L H_{11}^{(n)}] = H_{22}^{(n)} + r_L H_{21}^{(n)} \tag{4.25}$$

If $\boldsymbol{H}^{(n)}$ is expressed as $\boldsymbol{H}^{(n)} = \boldsymbol{T_p}^M$ where $\boldsymbol{T_p}$ is the matrix of one period, and M is the number of periods, (4.25) gives the threshold condition for DFB lasers [14]. As was shown in (3.26), $\boldsymbol{T_p}^M$ can be expressed analytically in terms of the matrix elements of $\boldsymbol{T_p}$.

4.3 Examples.

In the following examples, only TE modes are considered, and the overlap integrals of (2.9) and (2.17a) are assumed to be 1 for simplicity because this is usually a good approximation for a relatively shallow grating. Therefore, the relation (3.4) using Chebycheff polynomials (3.5) were used to calculate the total transfer matrix $\boldsymbol{T}_p^M$.

A. Conventional DFB lasers.

Consider a 1.3 μm DFB laser structure [11] as shown in Fig. 4.2. The structure consists of the active layer with thickness d_a and refractive index n_a, and the grating layer with thickness $d_g = d_H$ or d_L and refractive index n_g, which are sandwiched between the upper cladding layer with refractive index n_{cu} and the lower cladding layer with refractive index n_{cl}.

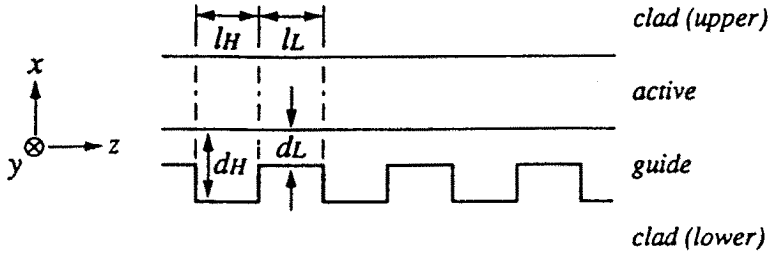

Figure 4.2 DFB laser structure with periodic variation in the thickness of the guiding layer.

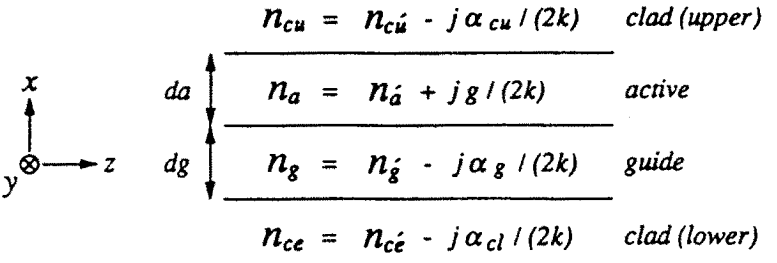

Figure 4.3 Four-layer waveguide structure.

(1) *Four-layer waveguide*

The transverse structure can be modeled as the four-layer waveguide shown in Fig. 4.3. The wave propagation is in the z direction. Only TE modes (y polarization) are considered for the sake of simplicity. First, the refractive indices are assumed real, and then the imaginary parts (gain or loss) are included as a perturbation. Following Hewak and Lit [21], we define for active and grating layers normalized thickness

$$V_a \equiv k_0 d_a (n_a^2 - n_{cl}^2)^{1/2} \tag{4.26}$$

$$V_g \equiv k_0 d_g (n_g^2 - n_{cl}^2)^{1/2} \tag{4.27}$$

where k_0 is the free space wavenumber. Also, we define the asymmetry factor

$$a \equiv (n_{cl}^2 - n_{cu}^2)/(n_z^2 - n_{cl}^2) \tag{4.28a}$$

and the normalized index

$$b = (N^2 - n_{cl}^2)/(n_a^2 - n_{cl}^2) \tag{4.28b}$$

where N is the effective index defined as

$$N = \beta/k_0 \tag{4.29}$$

β is the propagation constant for the guide mode. In addition, we define

$$h = (n_g^2 - n_{cl}^2)/(n_a^2 - n_{cl}^2) \tag{4.30}$$

Using the normalized parameters, the characteristic equation for the TE modes can then be expressed in the form [21]

$$V_a(1-b)^{1/2} = m_1\pi + \tan^{-1}\left(\frac{a+b}{1-b}\right)^{1/2} + \tan^{-1}\left(\left(\frac{h-b}{1-b}\right)^{1/2}\tan\left[\tan^{-1}\left(\frac{b}{1-b}\right)^{1/2} - V_g(h-b)^{1/2} + m_2\right]\right) \tag{4.31}$$

where $m_1, m_2 = 0, 1, 2, \cdots$. These two constants can be used to number the guided modes.

We now introduce the imaginary parts of n_a, n_g, n_{cl}, and n_{cu}. Writing $n_i = n_i' + n_i''(i = a, g, cl,$ and $cu)$ and $N = N' + N''$, and regarding n_i'' as a perturbation $(n_i'' << n_i')$, we can obtain, from (4.29) and (4.31) [21]

$$N'' = \sum_i \Gamma_i \frac{n_i'}{N'} n_i'' \qquad (i = a, g, cl, cu) \tag{4.32}$$

$$\Gamma_a = \frac{1}{\alpha}\left[V_a + \frac{\sin\phi}{2(1-b)^{1/2}} + \frac{(a+b)^{1/2}}{1+a}\right] \tag{4.33a}$$

$$\Gamma_g = \frac{1}{\alpha}\left[\tau\left(V_g + \frac{b^{1/2}}{h}\right) - \frac{\sin\phi}{2(h-b)}(1-b)^{1/2}\right] \tag{4.33b}$$

$$\Gamma_{cl} = \frac{\tau(h-b)}{hb^{1/2}} \tag{4.33c}$$

$$\Gamma_{cu} = \frac{1-b}{\alpha(1+a)(a+b)^{1/2}} \tag{4.33d}$$

where

$$\phi = 2\tan^{-1}\left(\left(\frac{h-b}{1-b}\right)^{1/2}\tan\left[\tan^{-1}\left(\frac{b}{1-b}\right)^{1/2} - V_g(1-b)^{1/2} + m_2\pi\right]\right) \tag{4.34a}$$

$$\alpha = V_a + \tau\left(\nu_g + \frac{1}{b^{1/2}}\right) - \frac{(1-h)\sin\phi}{2(1-b)^{1/2}(h-b)} + \frac{1}{(a+b)^{1/2}} \tag{4.34b}$$

$$\tau = \frac{1}{2}\left[1 + \left(\frac{1-b}{h-b}\right) - \left(\frac{1-b}{1-b}\right)\cos\phi\right] \tag{4.34c}$$

Γ_i can be shown to be the optical confinement factor for each layer [21]. Using the gain in the active layer, the absorption loss $\alpha_{abg}, \alpha_{abcl}$ and α_{abcu} in the grating, lower cladding, and upper cladding layers, respectively, we can express

$$n_a'' = jg/(2k_0), \qquad n_i'' = j\alpha_{abi}/(2k_0) \qquad (i = g, cl, cu) \tag{4.35}$$

Substitution of (4.35) into (4.32) yields

$$N'' = \frac{g_{eff}}{2k_0} = \frac{1}{2k_0}[\Gamma_{ae}g - \Gamma_{ge}\alpha_{abg} - \Gamma_{cle}\alpha_{abcl} - \Gamma_{cue}\alpha_{abcu}] \tag{4.36}$$

where

$$\Gamma_{ie} = \frac{n_i}{N}\Gamma_i \qquad (i = a, g, cu, cl) \tag{4.37}$$

and g_{eff} is the effective gain experienced by the propagating wave. For the symmetric three-layer case ($n_g = n_a$ and $n_{cl} = n_{cu} = n_c$), (4.36)

reduces to the following familiar expression if $n_a - n_c << n_c < n_a$ [22].

$$g_{eff} = \Gamma_a - (1 - \Gamma_a)\alpha_{abc} \tag{4.38}$$

where $\alpha_{abc} = \alpha_{abcu} = \alpha_{abcl}$.

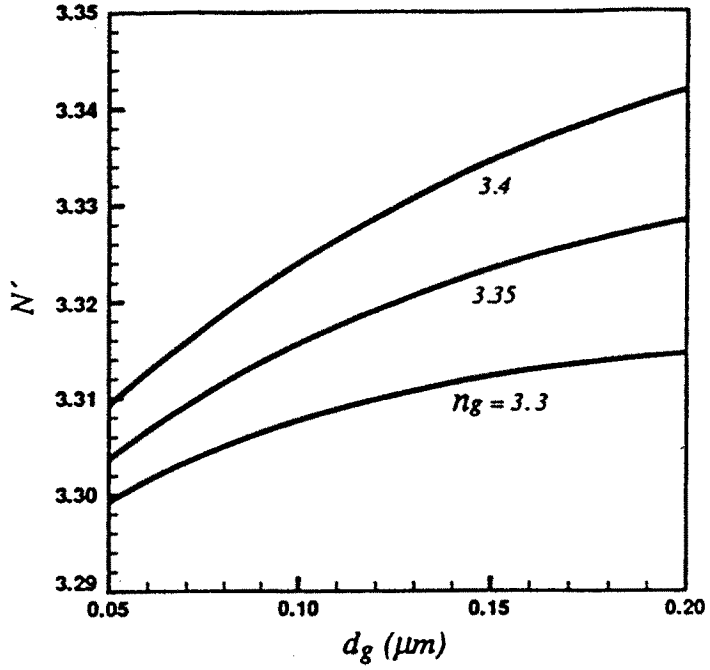

Figure 4.4 Effective index N' of the four-layer waveguide against the guiding layer thickness d_g.

Figure 4.4 shows the real part N' of the complex effective index as a function of d_g taking n'_g as a parameter for the case with $n'_a = 3.5, n'_{cu} = n'_{cl} = 3.2$, and $d_a = 0.2\mu$m. It is seen that the modulation of d_g gives rise to the modulation of N'. Figure 4.5 shows the effective confinement factors Γ_{ae}, Γ_{ge}, and $\Gamma_{ce} = \Gamma_{cue} = \Gamma_{cle}$, as a function of d_g taking n'_g as a parameter for the same parameters as in Fig. 4.4. It is obvious from Fig. 4.4 that the real effective index N'_H in the region with d_H is higher than the real effective index N'_L in the region with d_L. Therefore, the corrugation (the variation of d_g) introduces

the index periodicity. Denoting the effective gains corresponding to the regions with d_H and d_L by g_{effH} and g_{effL}, respectively, we can write, from (4.38),

$$g_{effL} - g_{effH} = (\Gamma_{aeL} - \Gamma_{aeH})g + (\Gamma_{geH} - \Gamma_{geL})\alpha_{abg} - (\Gamma_{ceL} - \Gamma_{ceH})\alpha_{abc} \tag{4.39}$$

It is obvious from Fig. 4.5 that $\Gamma_{ael} > \Gamma_{aeh}, \Gamma_{geh} > \Gamma_{gel}$, and $\Gamma_{cel} > \Gamma_{ceh}$. Because the third term in the right-hand side in (4.39) is usually small, we get $g_{effL} > g_{effH}$. Therefore, the corrugation introduces the effective gain periodicity, which is determined by the optical confinement factor in each layer. The loss in the guiding layer enhances the effective gain modulation, whereas the loss in the cladding layer reduces the effective gain modulation.

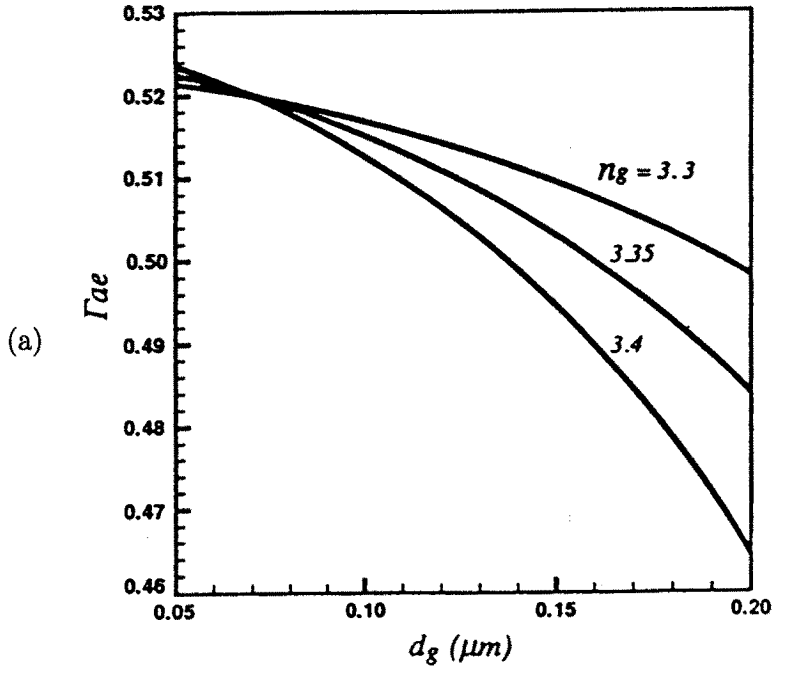

Figure 4.5 Effective optical confinement factors (a)Γ_{ae}, (b) Γ_{ge}, and (c) Γ_{ce}, in the active layer, the guiding layer, and the cladding layers, respectively, against the guiding layer thickness d_g with the guiding layer index n'_g as a parameter.

(b)

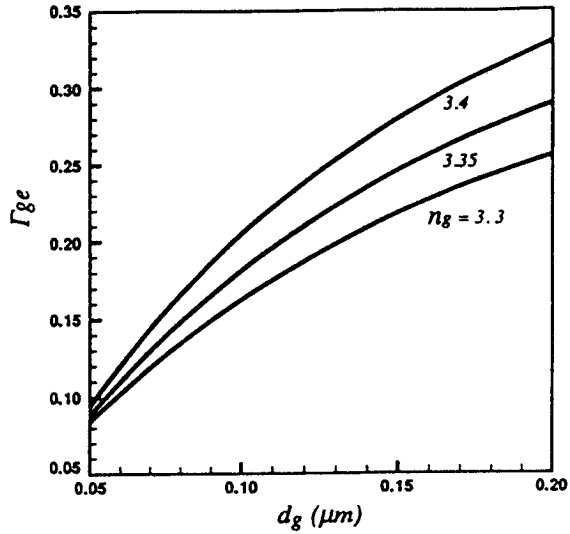

(c)

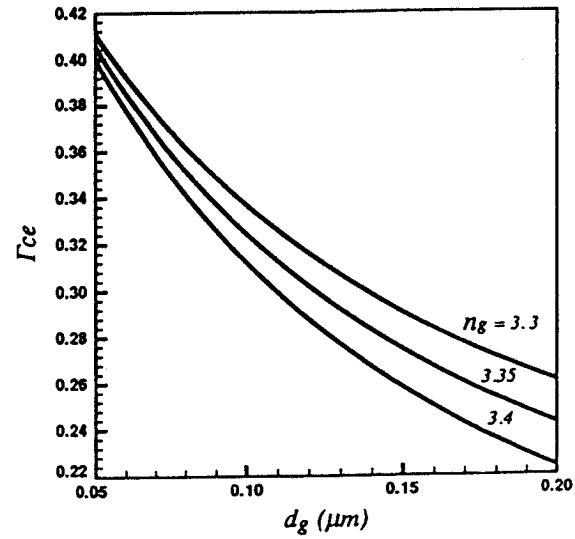

Figure 4.5 Effective optical confinement factors (a)Γ_{ae}, (b) Γ_{ge}, and (c) Γ_{ce}, in the active layer, the guiding layer, and the cladding layers, respectively, against the guiding layer thickness d_g with the guiding layer index n'_g as a parameter.

(2) *Threshold gain.*

1.3 μm DFB lasers are taken as examples in the following calculations: active , grating, and cladding layers consist of InGaAsP (1.3 μm), InGaAsP, and InP, respectively. A first-order grating is assumed (the Bragg wavelength is 1.3 μm), and the number of periods M is taken to be 1500 (the corresponding cavity length is 300 μm). d_H is assumed to be 0.2 μm, and the grating depth $\Delta d_g = d_H - d_L$ is taken as a variable.

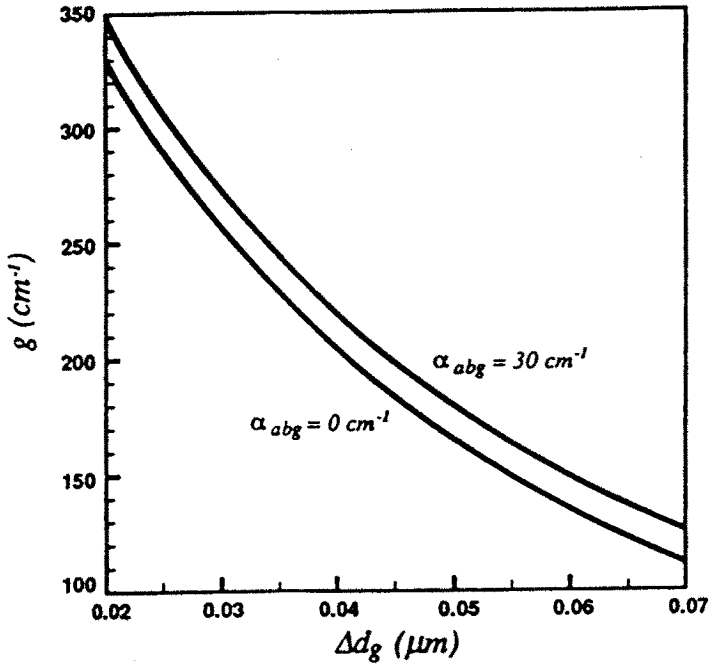

Figure 4.6 Threshold net power gain g of the mode +1 against the grating depth Δd_g in a 1.3 μm four-layer DFB laser with $n'_a = 3.5, n'_g = 3.3, n'_c = 3.2, d_a = 0.2\mu$m, $d_g = 0.2\mu$m, and $\alpha_{abc} = 0$. The absorption loss α_{abg} of the guiding layer is taken as a parameter.

Figure 4.6 shows the lowest threshold net power gain against Δd_g with the absorption loss α_{abg} in the grating layer as a parameter. The lowest and second-lowest threshold gains were always obtained for the + and - modes that are located just above and below the Bragg frequency, respectively. In Fig. 4.6, $n'_a = 3.5, n'_g = 3.3, n'_c = 3.2, d_a = 0.2\mu$ m, $d_g = 0.2\mu$m, and $\alpha_{abc} = 0$ are assumed. Figure 4.7 shows the normalized threshold gain gL and the normalized frequency deviation δL for the mode +1 where $\delta = (\omega_{+1} - \omega_0)/N'_H c, \omega_{+1}$ is the angular frequency of the mode +1, and ω_0 is the Bragg angular frequency. The horizontal axis is expressed by the normalized coupling coefficient instead of the grating depth. Figure 4.8(a) shows the threshold gain difference Δg between the modes +1 and -1 as a function of the grating depth Δd_g with the absorption loss α_{abg} in the grating layer as a parameter. The parameters are the same as in Fig. 4.6. It should be noted that there exists an inherent mode selectivity between the two modes +1 and -1 even if α_{abg} is zero. This can be explained by the gain periodicity, which is induced by the modulation of the effective optical confinement factor in the active layer as is seen from (4.39). Figure 4.8(a) also shows that the absorption loss α_{abg} in the grating layer increases the threshold gain difference. It is also noted from (4.39) that the gain (or loss) modulation is dependent on the effective optical confinement factors. Therefore, the waveguide parameters are expected to change these factors.

In Figure 4.8(b), a similar plot is shown where the parameters are the same as in Figure 4.8(a) except $n'_g = 3.4$. Figure 4.8(c) shows a similar plot where the parameters are the same as in Fig. 4.8(a) except $d_a = 0.1\mu$m. In Figure 4.8(d), a similar plot is shown where the parameters are the same as in Fig. 4.8(a) except $n'_g = 3.4$. It can be seen from comparisons between Fig. 4.8(a) and Fig. 4.8(b) and between Fig. 4.8(c) and (d) that a larger n'_g [3.4 in Fig. 4.8(b) and (d), whereas 3.3 in Fig. 4.8(a) and (c)] gives a larger Δg. This is explained as follows. A larger n_g causes a more rapid change of the effective confinement factors Γ_{ae} and Γ_{ge} against the grating layer thickness d_g [see Fig. 4.5(a) and (b)], therefore a larger gain modulation [see(15)]. The comparisons between Figs. 4.8(a) and (c) and between Figs. 4.8(c) and (d) indicate that a smaller d_a [0.1 μm in Figs. 4.8(c) and (d), whereas 0.2 μm in Figs. 4.8(a) and (b)] give a larger Δg. It has been confirmed that a smaller d_a causes a more rapid change of Γ_{ae} and Γ_{ge} against d_g. Therefore, we can conclude that in order to obtain a

larger threshold gain difference caused by gain and loss modulations, we need to design such a waveguide that the effective optical confinement factors for the active and grating layers could change rapidly against the change of the grating layer thickness.

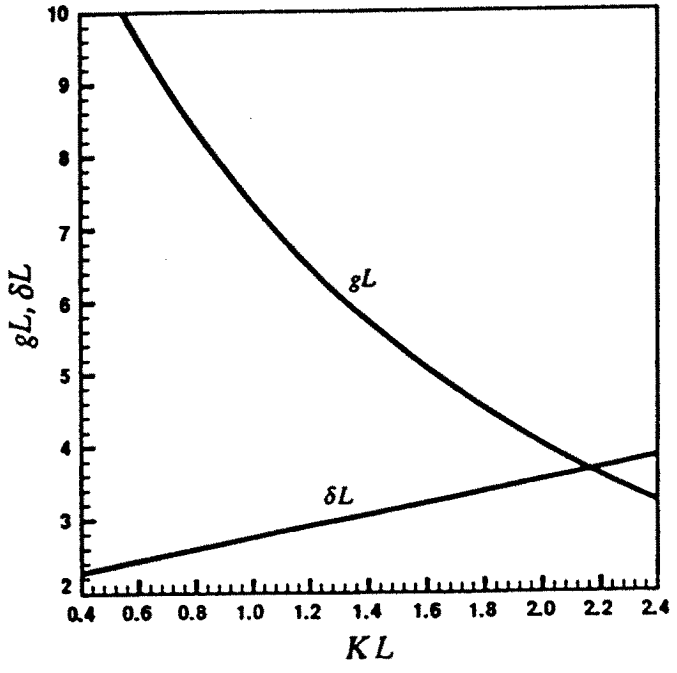

Figure 4.7 Normalized threshold gain gL and normalized frequency deviation δL against the normalized coupling coefficient κL for the same DFB laser as in Figure 4.6.

(a)

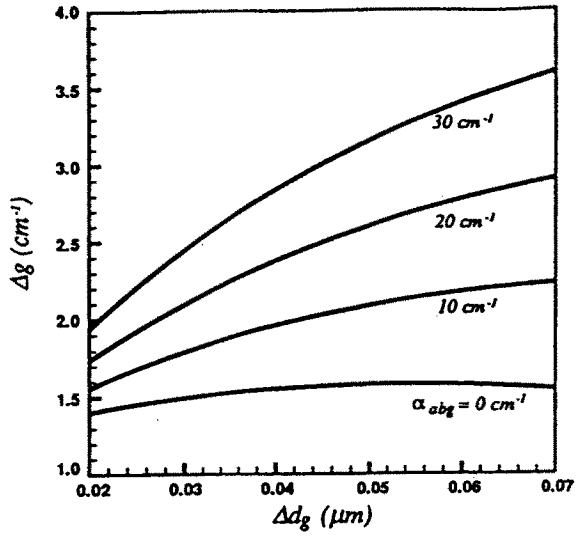

(b)

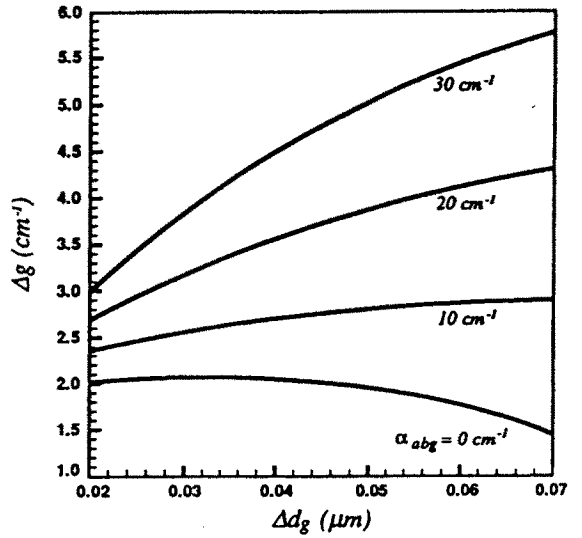

Figure 4.8 Dependence of the threshold gain difference Δg on the grating depth Δd_g. The absorption loss α_{abg} in the guiding layer is taken as a parameter. (a) $n'_a = 3.5, n'_g = 3.3, n'_c = 3.2, d_a = 0.2\mu$m, and $d_g = 0.2\mu$m. (b) $n'_a = 3.5, n'_g = 3.4, n'_c = 3.2, d_a = 0.2\mu$ m, and $d_g = 0.2\mu$m. $(c) n'_a = 3.5, n'_g = 3.3, n'_c = 3.2, d_a = 0.1\mu$m, and $d_g = 0.2\mu$m. $(d) n'_a = 3.5, n'_g = 3.4, n'_c = 3.2, d_a = 0.1\mu$m, and $d_g = 0.2\mu$m.

(c)

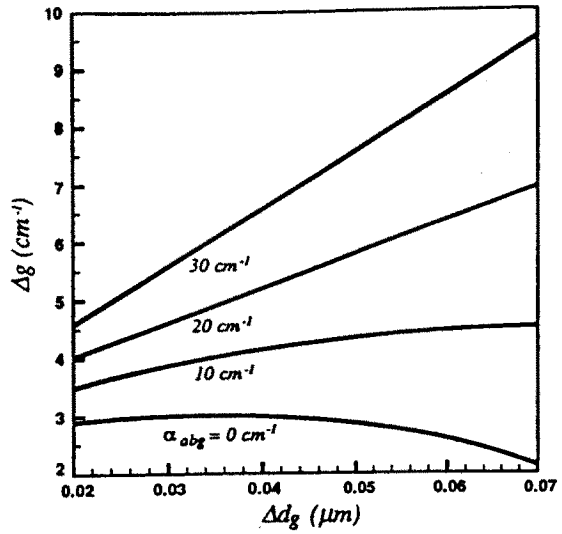

(d)

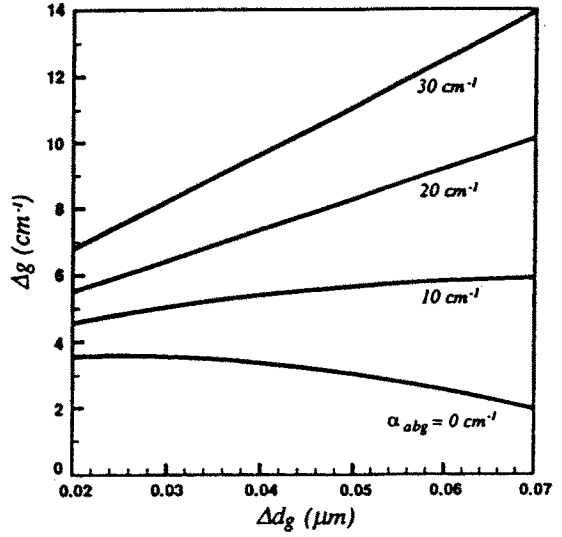

Figure 4.8 Dependence of the threshold gain difference Δg on the grating depth Δd_g. The absorption loss α_{abg} in the guiding layer is taken as a parameter. (a) $n_a' = 3.5, n_g' = 3.3, n_c' = 3.2, d_a = 0.2\mu$m, and $d_g = 0.2\mu$m. (b) $n_a' = 3.5, n_g' = 3.4, n_c' = 3.2, d_a = 0.2\mu$ m, and $d_g = 0.2\mu$m. $(c) n_a' = 3.5, n_g' = 3.3, n_c' = 3.2, d_a = 0.1\mu$m, and $d_g = 0.2\mu$m. $(d) n_a' = 3.5, n_g' = 3.4, n_c' = 3.2, d_a = 0.1\mu$m, and $d_g = 0.2\mu$m.

(3) *Discussion.*

Kapon et al. [23] have analyzed the threshold gain for DFB lasers with complex-coupling coefficients and showed that the threshold gain difference between the +1 and -1 modes increases from zero as the imaginary part of the complex coupling coefficient increases from zero. The structure in Fig. 2 actually corresponds to the case with complex coupling coefficient. Nakano et al. [24] proposed gain-coupling DFB lasers in which gain periodicity is incorporated by loading periodic loss perturbation. They demonstrated single longitudinal-mode oscillation at the +1 mode. It is noted from (4.39) that the loss in the grating layer increases the gain modulation.

B. MQW DFB lasers.

MQW DFB lasers have many advantages over the conventional double heterostructure such as narrow linewidth, low chirping, low threshold current, high output power and high frequency response [8]. The design of MQW DFB lasers is very complicated because the structure consists of many layers and gratings. Moreover, the complexity is caused by the cavity loss being dependent on the number of quantum wells because the grating coupling coefficient is also a function of the number of wells (the cavity loss in Fabry-Perot lasers is given by $1/Lln(1/R)$ where L is the cavity length and R is the facet reflectivity).

We give a 3D analysis of InGaAs/InGaAsP BH MQW DFB lasers. The threshold gain is analyzed as a function of the number of quantum wells, taking the BH stripe width as a parameter.

Consider a BH MQW DFB laser illustrated schematically in Fig. 4.9. The structure consists of quantum wells of thickness W_w, barrier of thickness W_b, a separate confinement (SC) layer of thickness W_{sc}, and a grating layer with alternating thickness d_H and d_L. The effective indices n_H and n_L of the corrugation sections with d_H and d_L can be found from the eigenvalue equation for the propagation constant of the corresponding multilayer waveguide. The eigenvalue equation for the propagation constant β of a N-layer waveguide can be expressed as follows [25]. S_i is the characteristic matrix in the ith layer $(i = 1, \ldots, N)$, and is given by

$$[\gamma_c \quad 1][S_N S_{N-1} \ldots S_2 S_1]\begin{bmatrix} 1 \\ \gamma_c \end{bmatrix} = 0 \tag{4.40}$$

$$S_i = \begin{bmatrix} \cos \xi_i d_i & 1/\xi_i \sin \xi_i d_i \\ -\xi_i \sin \xi_i d_i & \cos \xi_i d_i \end{bmatrix} \tag{4.41}$$

where $\xi_i = (k_0 n_i^2 - \beta^2)^{1/2}$, n_i and d_i are the refractive index and the thickness of the i th layer, respectively. k_0 is the free space wavenumber and $\xi_c = j/\gamma_c$ with the subscript c denoting the clad layer. Here, TE modes are assumed . For a quantum well, n_i can be expressed as

$$n_i = n_i' + j\frac{g}{2k_0} \tag{4.42}$$

where n_i' is the real refractive index, and g is the material (power) gain. The propagation constant $\beta_s (s = H, L)$ defines the effective refractive index by

$$n_s = \beta/k_0 = n_s' + jn_s'' = n_s' + \frac{jg_s}{2k} \qquad (s = H, L) \tag{4.43}$$

where g_H and g_L are the modal (power) gains in the sections H and L, respectively.

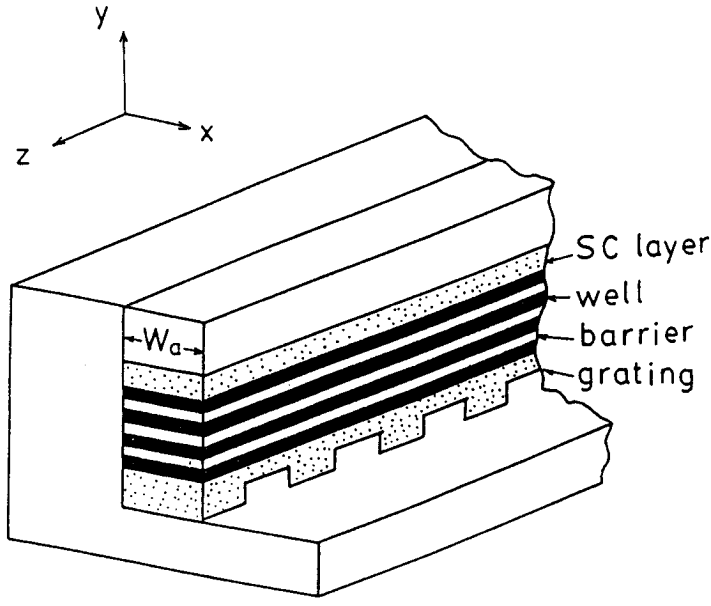

Figure 4.9 Schematic diagram of BH MQW DFB laser.

As a numerical example, we take a 1.55 μm $\lambda/4$-shifted MQW DFB laser consisting of InGaAs ($\lambda_g = 1.65\mu$m) wells and InGaAsP ($\lambda_g = 1.3\mu$m) barriers and an SC layer and an InGaAsP ($\lambda_g = 1.3\mu$m) grating layer. The thickness of each layer has been assumed to be as follows: $W_w = 70\mathring{A}, W_b = 100\mathring{A}, W_{sc} = 100\mathring{A}, d_H = 2000\mathring{A}$, and $d_L = 1700\mathring{A}$. The absorption losses in the well and the other regions have been assumed to be 40 cm^{-1} and 5 cm^{-1}, respectively. The grating depth has been assumed to be 300 $\mathring{A}$. The dependence of the optical peak gain on current density can be expressed by a close approximation [26].

$$g = g_0 \ln(J/J_0) \tag{4.44}$$

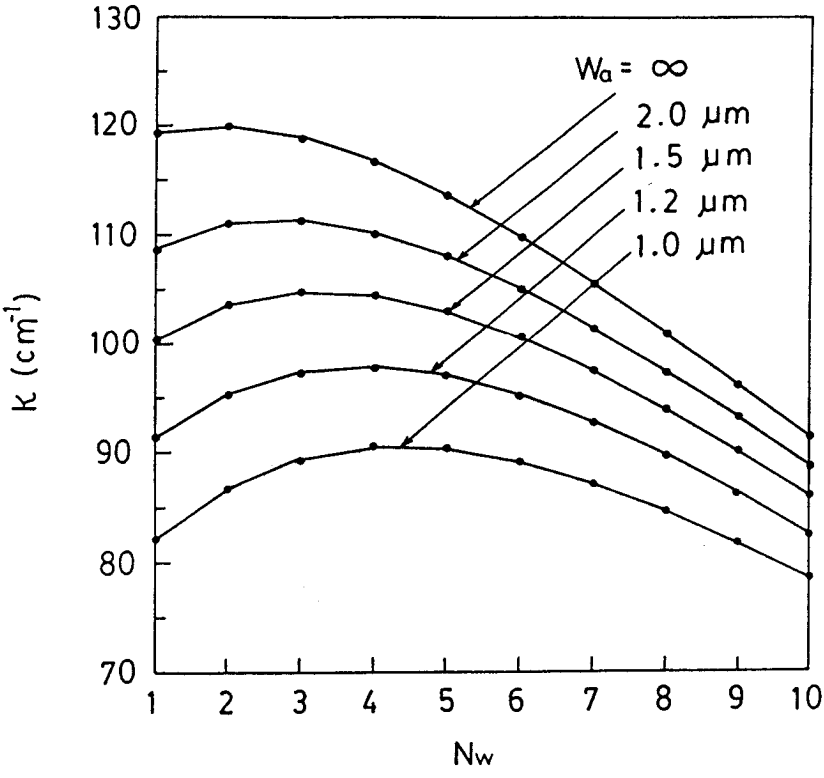

Figure 4.10 Coupling coefficient κ as a function of number of wells N_w with active layer width W_a as a parameter.

We have used the values of $g_0 = 516.6\,\mathrm{cm}^{-1}$ and $J_0 = 53\,\mathrm{Acm}^{-2}$ [26] for the calculation. Figure 4.10 shows the grating coupling coefficient κ as a function of the number of wells N_w, taking active layer width W_a as a parameter. Figure 4.11 is a similar plot for the threshold current density J_{th} for the cavity length $L = 300\,\mu\mathrm{m}$. It is seen that J_{th} becomes minimum at a certain number of wells, similarly to MQW Fabry-Perot lasers. It should be noted that the number of wells giving the minimum J_{th} becomes larger as W_a decreases. This can be explained by the fact that the optical confinement factor decreases as W_a decreases because the optical confinement along the lateral decreases.

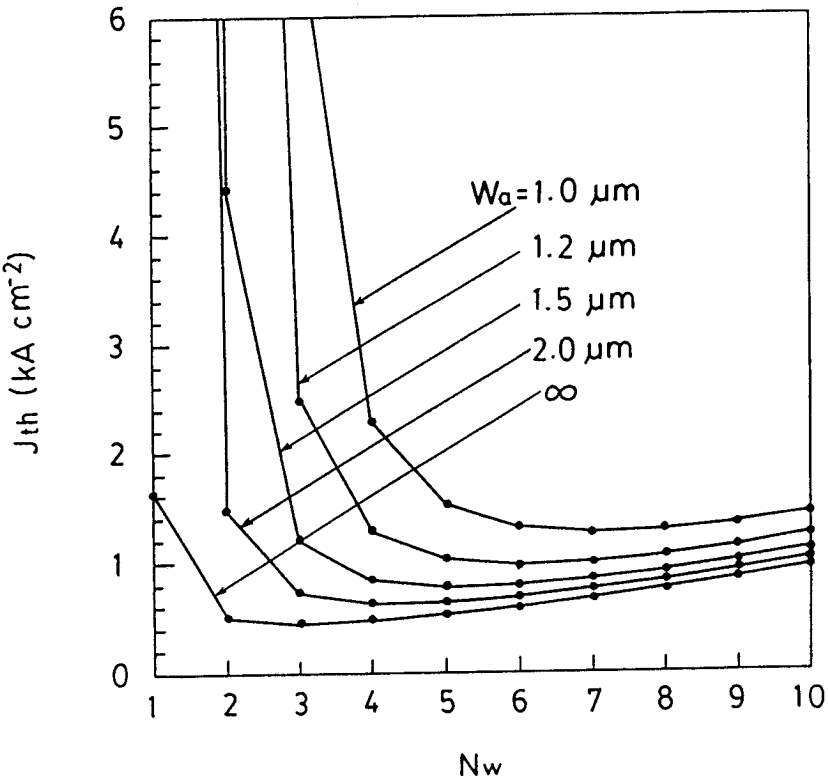

Figure 4.11 Threshold current density J_{th} as a function of number of wells N_w with active layer width W_a as a parameter.

C. Vertical cavity surface-emitting lasers.

Vertical cavity surface-emitting (SE) semiconductor lasers offer a number of advantages, such as low divergence output beams desired for efficient coupling into optical fibers, and inherent single-longitudinal-mode operation due to the large mode spacing arising from a short cavity length. They can be tested on the wafer, and can provide high density 2-D self-aligned arrays. SE semiconductor lasers can be divided into three types; Fabry-Perot (FP) [27], distributed Bragg reflector (DBR) [28], and distributed feedback (DFB) [29,30] structures. Among these, SE DFB lasers have a number of unique features. In a SE DFB laser, the grating consists of an alternating sequence of active and passive layers deposited during epitaxial growth. The active and passive epitaxial layers can differ in refractive index by more than 10 %, and this results in a very large index coupling coefficient. In addition to a large coupling coefficient, a SE laser has the feature that a phase shift layer can be simply and accurately introduced by increasing the thickness of one layer. A DFB laser with a $\lambda/4$ phase shift layer will oscillate exactly at the Bragg wavelength [30], and so with excellent epitaxial layer composition and thickness control, we expect that a SE DFB laser can be fabricated with very good wavelength selectivity.

(1) *Standard SE DFB laser* [15].

As a first example, we analyze a $1.3\,\mu$m InGaAsP-InP DFB laser. The active layers are InGaAsP ($\lambda_g = 1.3\,\mu$m), and the passive layers are InP. The refractive indices of the active layers and the passive layers are denoted by n_H and n_L, respectively, and the layer sequence is assumed to be $n_H n_L \ldots n_H n_L n_H$ from the bottom to the top in Fig. 4.12. In the following, laser parameters n_{sp}, ν_g, α_H, and g are used for brevity for the layer with n_H. The parameter values used for the calculations are listed in Table I [27,31]. The end refelctivities were assumed to be zero for the sake of simplicity.

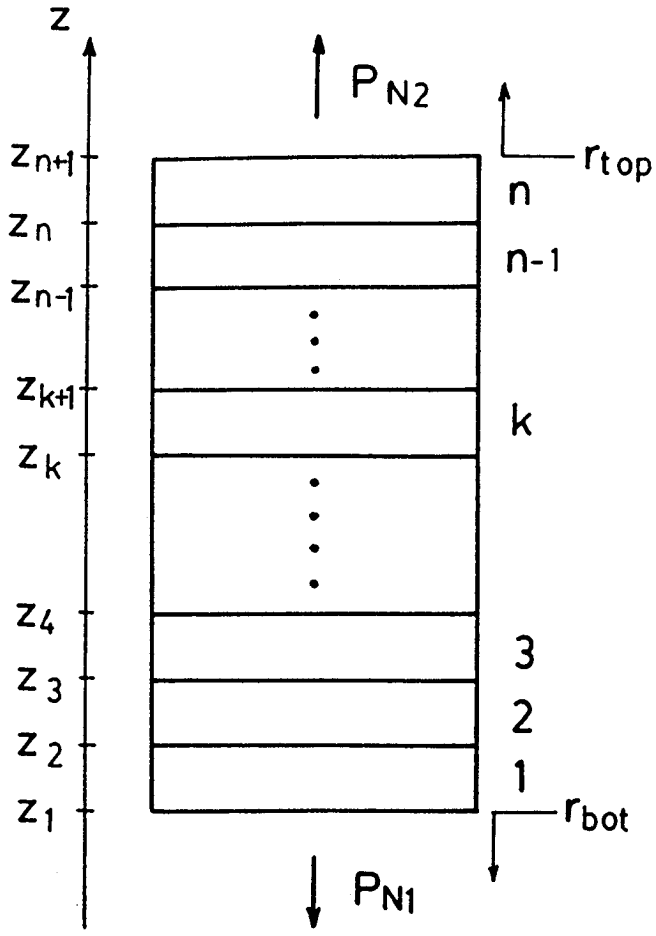

Figure 4.12 Schematic diagram of a SE DFB semiconductor laser.

parameter	symbol	value
Bragg wavelength		1.3 μm
refractive indices		
active in GaAsP (λ_g=1.3 μm)	n_1	3.5
passive InGaAsP (λ_g=1.2 μm)	n_2	3.41
InP		3.2
absorption losses		
active InGaAsP (λ_g=1.3 μm)		50 cm^{-1}
passive InGaAsP (λ_g=1.2 μm)		10 cm^{-1}
InP		10 cm^{-1}
gain slope	A_0	2.5×10^{-16} cm^2
carrier density at transparency	N_0	1.5×10^{18} cm^{-3}
effective recombination constant	B_{eff}	1.0×10^{-10} $cm^3 s^{-1}$
linewidth enhancement factor	α_H	6
average group velocity	v_g	$3 \times 10^{10}/4$ cm s^{-1}

Table 1. List of parameter values.

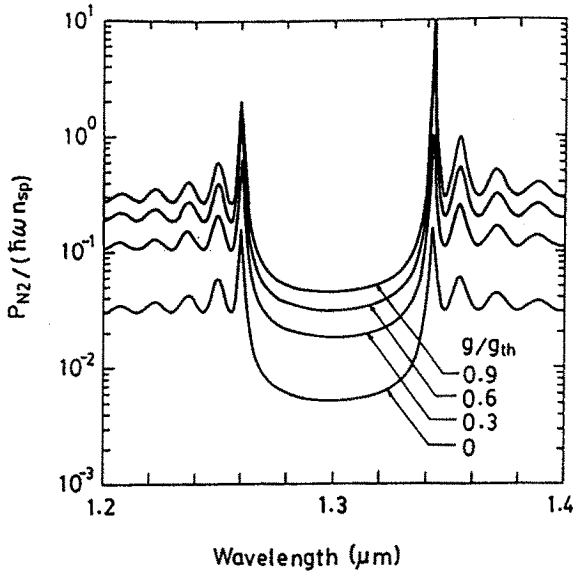

Figure 4.13 Normalized spontaneous emission spectrum below lasing threshold for a SE DFB consisting of 141 layers. The normalized gain g/g_{th} is taken as a parameter.

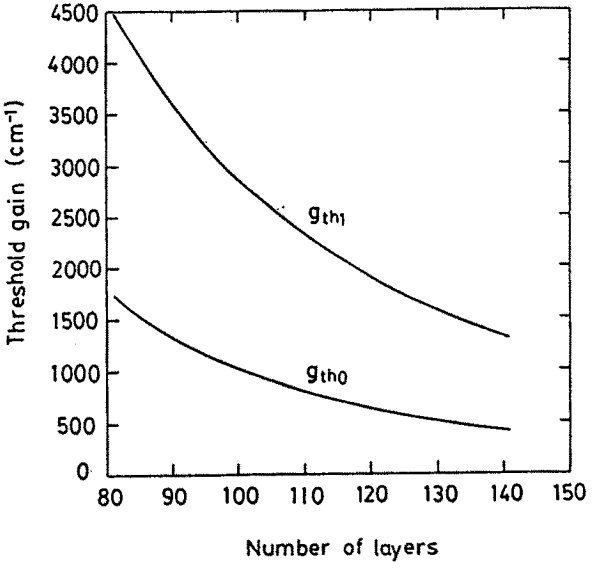

Figure 4.14 Lowest (g_{th0}) and second lowest (g_{th1}) threshold (net power) gains against the total number of layers of a SE DFB laser.

Figure 4.13 shows the normalized spontaneous emission spectrum below threshold for a total of 141 layers with the normalized gain g/g_{th} as a parameter, where g_{th} is the threshold (net power) gain. Here we have assumed that the material gain, the absorption loss, and the refractive index are independent of wavelength in order to emphasize the DFB effect: The wavelength dependence of the spontaneous emission arises from that of a periodic structure, but not from that of those material parameters. Hamasaki and Iwashima [32] have shown that the transmission and reflection coefficients of a SE DFB laser have a single sharp peak at the long-wavelength edge of the Bragg band, and a suppressed gain at the short-wavelength edge. It should be pointed out that although the transmission coefficient has a similar frequency dependence to that of spontaneous emission [32,33], a proper spontaneous emission model must be used to simulate the below threshold spectrum of a DFB laser [13]. It is seen from Fig. 4.13 that as the gain increases, the two peaks at the Bragg band edges initially grow approximately equally, and then the mode at the long-wavelength edge rises faster and reaches threshold first. Conventional DFB lasers with index coupling have a symmetrical spontaneous emission spectrum [13], and the mode at the short wavelength side and the long-wavelength side of the Bragg band have the same threshold gain [7]. However,once a gain periodicity is incorporated, one of the two modes has a lower threshold gain than that of the other mode [23]. Figure 4.14 shows the calculated lowest and second lowest threshold gains for our SE DFB structure against the total number of layers.

(2) *SE $\lambda/4$-shifted DFB laser with a DBR mirror* [15].

As a second example, consider a $\lambda/4$-shifted SE DFB laser with a DBR mirror on the bottom as shown schematically in Fig. 4.15. The structure has a DFB region which consists of alternating active InGaAsP ($\lambda_g = 1.3\mu$m) and InP layers, and a DBR mirror which consists of passive InGaAsP ($\lambda_g = 1.2\mu$m) and InP layers. We have used the parameter values listed in Table I for the calculations. The thickness of each layer is quarter wavelength except that a half wavelength layer is used as a $\lambda/4$ phase-shift layer in the middle of the DFB region. A DBR mirror of 36 pairs was assumed, giving a power reflection coefficient $R_{DBR} = |r_{DBR}|^2$ (see Figure 4.15) of 0.95. The material below the DBR mirror was assumed to be InP.

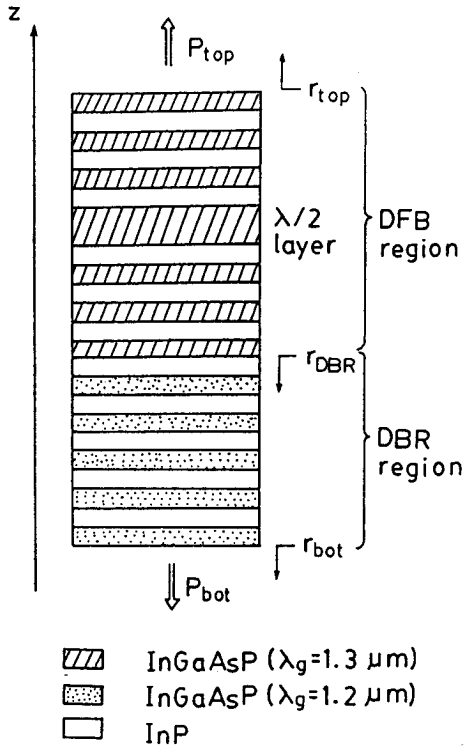

Figure 4.15 Schematic diagram of a SE λ/4-shifted DFB laser with a DBR mirror.

Figure 4.16 shows the normalized spontaneous emission spectrum below threshold when the DFB region consists of 41 layers. The material parameters were assumed to be independent of the wavelength for the same reason as explained in the first example. In Figure 4.17, the threshold (net power) gain of the lowest mode is shown as a function of the total number of layers N_t in the DFB region, taking $R_{top} = |r_{top}|^2$ as a parameter. For comparison, the threshold gain in the case that the InP layers in the DFB region are replaced by InGaAsP active layers, giving a laser with a homogeneous-active region (which we shall refer to subsequently as the homogeneous-active structure), is shown by the dashed curve in Fig. 4.17. In all the cases considered for the DFB-active and homogeneous active structure, the resonance mode with the lowest threshold gain was obtained at the Bragg wavelength.

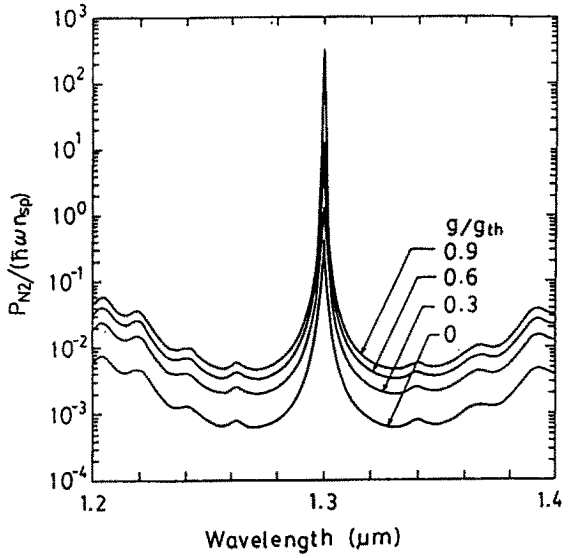

Figure 4.16 Normalized spontaneous emission spectrum below lasing threshold for a SE $\lambda/4$-shifted DFB laser with a DBR mirror. The number of layers in the DFB region is 41. The DBR mirror consists of 36 periods ($R_{DBR} = 0.95$).

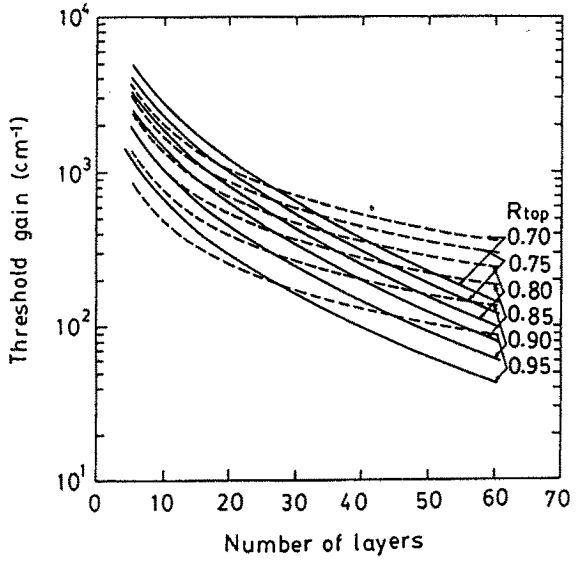

Figure 4.17 Lowest threshold gain against the number of layers in the DFB region. The cases with periodic and homogeneous active regions are shown by the solid and dashed curves, respectively. The DBR mirror consists of 36 periods ($R_{DBR} = 0.95$).

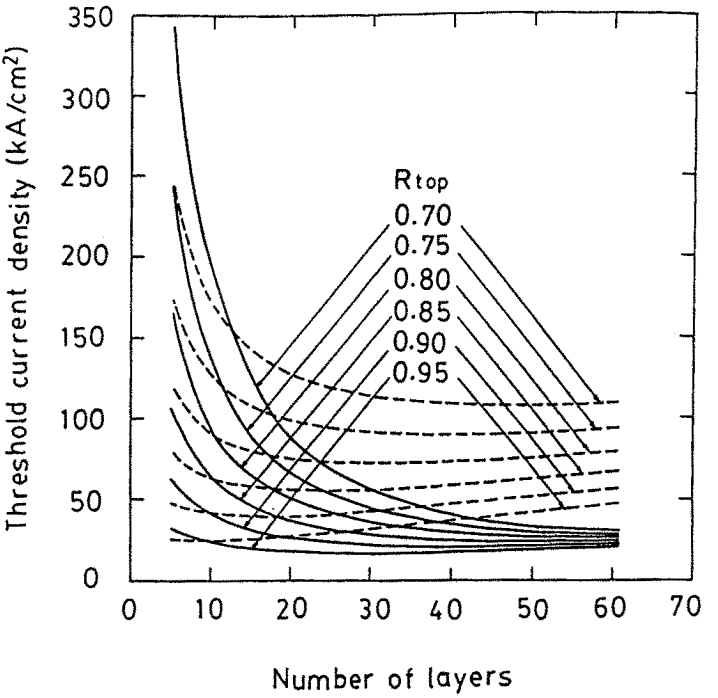

Figure 4.18 Threshold current density against the number of layers in the DFB region. The parameters are the same as in Figure 4.17.

The threshold current density J_{th} can be expressed as [34]

$$J_{th} = J_{nom} N_a d_a / \eta_{int} \tag{4.45a}$$

$$J_{nom} = eB_{eff}(g_{th}/A_0 N_0)^2 \tag{4.45b}$$

where N_a is the number of active layers, d_a is the active layer thickness, η_{int} is the internal quantum efficiency, e is the electron charge, B_{eff} is the effective recombination constant, $g_{th} = 2\alpha_H + \alpha_{ab}$ is the threshold power gain where α_{ab} is the absorption loss of the active layer, and A_0 and N_0 are the parameters expressing the peak gain g_p as a function of carrier density N by $g_p = A_0(N - N_0)$. Here we have assumed that the laser oscillates at the gain peak for the sake of simplicity ($g_{th} = g_p$).

Figure 4.18 shows the threshold current density J_{th} (solid curve) as a function of N_t, taking R_{top} as a parameter. For comparison, the threshold current density for the homogeneous-active structure is shown by the dashed curve in Fig. 4.18. It is noted from Fig. 4.18 that for a small number of active layers the homogeneous-active structure gives a lower threshold current density than the DFB -active structure, while for a large number of active layers the DFB-active structure gives a lower threshold current density for all R_{top}. The lowest threshold current density is achieved by the DFB-active structure, and the threshold current density becomes less sensitive to R_{top} as the number of active layers increases, because of the DFB effect.

This behavior can be explained from (4.45) as follows. There are two competing N_a-dependent factors in J_{th} : g_{th} decrease as N_a increases and J_{th} is proportional to N_a. The decrease of g_{th} with increasing N_a is faster in The DFB-active structure than in the homogeneous-active structure because of the increasing distributed feedback effect in the former. In the DFB-active structure, the decrease of J_{nom} due to the decrease of g_{th} in (4.45b) overwhelms the linear increase of J_{th} with N_a in (4.45a), resulting in a net decrease of J_{th}.

5. Conclusions

The transfer matrix method (TMM) and its application to DFB semiconductor lasers have been discussed. The transfer matrix for corrugation discontinuities in a corrugated waveguide has first been derived, and then used to obtain analytical expressions of the transfer matrix for a whole DFB waveguide structure. The TMM has been compared to the coupled mode theory (CMT), and the CMT result has been shown to be reproduced by the TMM under an assumption of weak grating perturbation.

For the application of the TMM to DFB semiconductor lasers, the TMM has been extended to incorporate the spontaneous emission noise by combining with the Green's function method. Then, as numerical examples, the TMM has been applied to the threshold analysis of bulk active-layer semiconductor lasers and MQW DFB lasers. Applications to vertical-cavity surface-emitting DFB/DBR lasers are also discussed.

In this chapter, the TMM has been applied to only the threshold analysis of DFB semiconductor lasers. In order to analyze dynamic

characteristics such as modulation speed and intensity/phase noise, TMM dynamic rate equations must be used as well as a carrier rate equation. More advanced carrier rate equations are required for MQW DFB lasers to take into account carrier transport effects in quantum wells.

References

1. Yariv, A., and M. Nakamura, "Periodic structures for integrated optics," *IEEE J. Quantum Electron.*, Vol. QE-13, 233-=253, Apr. 1977.
2. Yariv, A., "Coupled-mode theory for guided-wave optics," *IEEE J. Quantum Electron.*, Vol. QE-9, 919–933, Sept. 1973.
3. Streifer, W., D. R. Scifres, and R. D. Burnham, "Coupling coefficient for distributed feedback single- and double heterostructure diode lasers," *IEEE J. Quantum Electron.*, Vol. QE-11, 867–873, Nov. 1975.
4. Streifer, W., D. R. Scifres, and R. D. Burnham, "TM-mode coupling coefficient in guided-wave distributed feedback lasers," *IEEE J. Quantum Electron.*, Vol. QE-12, 74–78, Feb. 1976.
5. Hall, D. G., "Coupled-mode theory for corrugated optical waveguides," *Opt. Lett.*, Vol. 15, 619–621, Nov. 1990.
6. Agrawal, G. P., and N. K. Dutta, *Long-wavelength Semiconductor Lasers,* New York, Van Nostrand Reinhold, Ch. 6, 1986.
7. Kogelnik, H., and C. V. Shank, "Coupled-wave theory of distributed feedback lasers," *J. Appl. Phys.*, Vol. 43, 2327–2335, May 1972.
8. Makino, T., "Three-dimensional analysis of multiquantum well DFB lasers," *Electron. Lett.*, Vol. 27, 1118–1119, June 1991.
9. Yamada, M., and K. Sakuda, "Analysis of almost-periodic distributed feedback slab waveguides via fundamental matrix approach," *Appl. Opt.*, Vol. 26, 3474–3478, Aug. 1987.
10. Björk, G., and O. Nelsson, "A new exact and efficient numerical matrix theory of complicated laser structures; properties of asymmetric phase-shifted DFB lasers," *J. Lightwave Technol.*, Vol. LT-5, 140–146, Jan. 1987.
11. Makino, T., "Effective-index matrix analysis of distributed feedback semiconductor lasers," *IEEE J. Quantum Electron.*, Vol. 28, 434–440, Feb. 1992.

12. Born, M., and E. Wolf, *Principles of Optics,* Pergamon Press, 3rd edition, 1965.
13. Makino, T., and J. Glinski, "Transfer matrix analysis of the amplified spontaneous emission of DFB semiconductor laser amplifiers," *IEEE J. Quantum Electron.,* Vol. QE-24, 1507–1518, 1988.
14. Makino, T., "Transfer-matrix formulation of spontaneous emission noise of DFB semiconductor lasers," *J. Lightwave Technol.,* Vol. 9, 84–91, Jan. 1991.
15. Makino, T., "Spontaneous emission model of surface-emitting DFB semiconductor lasers," *IEEE J. Quantum Electron.,* Vol. 29, 14–22, Jan. 1993.
16. Wang, S., "Proposal of periodic layered waveguide structures for distributed lasers," *J. Appl. Phys.,* Vol. 44, 767–780, Feb. 1973.
17. Hardy, A., "Exact derivation of the coupling coefficient in corrugated waveguides with rectangular tooth shape," *IEEE J. Quantum Electron.,* Vol. QE-20, 1132–1139, Oct. 1984.
18. Hong, J., W. P. Huang, and T. Makino, "On the transfer matrix method for distributed-feedback waveguide devices," *J. Lightwave Technol.,* Vol. 10, 1860–1868, Dec. 1992.
19. Yeh, P., A. Yariv, and C. Hong, "Electromagnetic propagation in periodic stratified media, I. general theory," *J. Opt. Soc. Amer.,* Vol. 67, 423–438, Apr. 1977.
20. Henry, C. H., "Theory of spontaneous emission noise in open resonators and its application to lasers and optical amplifiers," *J. Lightwave Technol.,* Vol. LT-4, 288–297, Mar. 1986.
21. Hewak, D. W., and J. W. Lit, "Generalized dispersion properties of a four-layer thin-film waveguide," *Appl. Opt.,* Vol. 25, 1977–1981, June 1986.
22. Buus, J., "The effective index method and its application to a semiconductor lasers," *IEEE J. Quantum Electron.,* Vol. QE-18, 1083–1089, July 1982.
23. Kapon, E., A. Hardy, and A. Kazir, "The effect of complex coupling coefficients on distributed feedback lasers," *IEEE J. Quantum Electron.,* Vol. QE-18, 66–71, Jan. 1982.
24. Nakano, Y., Y. Luo, and K. Tada, "Facet reflection independent single longitudinal mode oscillation in a GaAlAs/GaAs distributed feedback laser equipped with a gain coupling mechanism," *Appl. Phys. Lett.,* Vol. 55, 1606–1608, Oct. 1989.

25. Ramadas, M. R., E. Garmire, A. K. Ghatak, K. Thyagarajian, and M. R. Shenoy, "Analysis of absorbing and leaky planar waveguides: a novel method," *Opt. Lett.*, Vol. 14, 376–378, Apr. 1989.
26. Rosenweig, M, M. Möhrle, H. Düser, and Venghaus, "Threshold-current analysis of InGaAs-InGaAsP multiquantum well separate-confinement lasers," *IEEE J. Quantum Electron.*, Vol. 27, 1804–1811, June 1991.
27. Iga, K., and S. Uchiyama, "GaInAsP-InP surface-emitting laser diode," *Opt. Quantum Electron.*, Vol. 18, 403–422, 1986.
28. Yang, Y. J., T. G. Dziura, S. C. Wang, W. Hsin, and S. Wang, " Submiliampere continuous-wave room temperature lasing operation of a GaAs mushroom structure surface-emitting laser," *Appl. Phys. Lett.*, Vol. 56, 1839–1840, May 1990.
29. Uchiyama, S., K. Iga, and Y. Kokubun, "Threshold gain of distributed feedback surface emitting lasers," *Proc. 12th Euro. Conf. Opt. Commun.*, Barcelona, Spain, paper MB4 Telefonica, 1986.
30. Ogura, M., W. Hsin, M. C. Wu, S. Wang, J. R. Whinnery, S. C. Wang, and J. J. Yang, "Surface-emitting laser diode with vertical GaAs/GaAlAs quarter-wavelength multilayers and lateral buried heterostructure," *Appl. Phys. lett.*, Vol. 51, 1655–1657, Nov. 1987.
31. Henry, C. H., L. F. Johnson, R. A. Logan, and D. P. Clark, "Determination of the refractive index of InGaAsP epitaxial layers by mode line luminescence spectroscopy," *IEEE J. Quantum Electron.*, Vol. QE-21, 1887–1892, Dec. 1985.
32. Hamasaki, J., and T. Iwashima, "A single-wavelength DFB structure with a synchronized gain profile," *IEEE J. Quantum Electron.*, Vol. 24, 1864–1872, Sept. 1988.
33. Dziura, T. G., and S. C. Wang, "Emission properties of surface-emitting distributed-feedback and distributed-Bragg-reflector semiconductor lasers," *Opt. Lett.*, Vol. 14, 491–493, May 1989.
34. Corzine, S. W., R. S. Geels, F. W. Scott, R. Yan, and L. A. Coldren, "Design of Fabry-Perot surface-emitting lasers with a periodic gain structure," *IEEE J. Quantum Electron.*, Vol. 25, 1513–1524, June 1989.
35. Makino, T., "Transfer-matrix theory of the modulation and noise of multielement semiconductor lasers," to be published in *IEEE J. Quantum Electron*, Vol. 29, 2762–2770, Nov. 1993.